JOURNAL OF CATALYSIS 127, 524–552 (1991)

Kinetics and Multiple Rate States of CO Oxidation on Pt

I. Model Development and Multiplicity Analysis

MICHAEL P. HAROLD* AND MARTHA E. GARSKE

Department of Chemical Engineering, University of Massachusetts, Amherst, Massachusetts 01003

Received December 28, 1989; revised September 19, 1990

This first of a two-part study focuses on the kinetics and rate multiplicity features of CO oxidation on Pt. The objective is to formulate models that predict the kinetics and rate multiplicity features observed by experimentalists over a wide range of catalyst temperature, gas composition, and total pressure. It is demonstrated that the commonly used three-step sequence (model I), consisting of reversible CO adsorption, dissociative oxygen adsorption, and a Langmuir reaction step, capably predicts multiplicity features observed under UHV conditions, such as the shape of the multiplicity region (bifurcation map) in the catalyst temperature–CO pressure plane. A method is presented in which parameter space is divided into regions in which different shapes of temperature–CO pressure bifurcation maps are encountered. This scheme provides a useful means of checking if a model can predict the qualitative multiplicity features, and of bounding parameter values based on the shape of the bifurcation map. It is shown that model I cannot predict the correct CO reaction order in the limits of low and high CO pressure, or the apparent activation energy in the CO inhibition regime. Thus, prediction of the multiplicity features alone is insufficient. Four new kinetic models built upon the model I framework are developed and analyzed. Model II contains three additional steps involving molecularly adsorbed oxygen and reaction steps between gas phase CO and adsorbed oxygen species. Oxygen may adsorb by a direct dissociative route or by a two-step molecular precursor route. Model III consists of the three model I steps, the three model II molecular oxygen steps, and an oxygen site exclusion feature. Model IV incorporates site exclusion for CO and oxygen into the three model I steps. Model V has a structure similar to model II, the main difference being that oxygen adsorption proceeds only by an equilibrated molecular adsorption step and irreversible dissociation. Our analyses show that the three steps involving molecular oxygen (models II, III, and V) or CO site exclusion (model IV) remedy the incorrect model I predictions in the CO inhibition regime. Moreover, the Eley–Rideal type reactions (models II and V) or oxygen site exclusion (models II and IV) remedy the incorrect model I predictions of the CO reaction order for the oxygen covered surface. Bifurcation map constructions also demonstrate that each model can predict the correct qualitative multiplicity features.

INTRODUCTION

Carbon monoxide oxidation on noble metal catalysts has been the subject of a large number of surface science and kinetics studies. Its importance in automobile emission control aside (*2*), the intriguingly rich behavior of this seemingly simple reaction promotes new studies. Engel and Ertl (*3*) reviewed the findings of ultrahigh vacuum (UHV) studies of the elementary steps.

The more recent UHV and higher pressure studies have focused on three areas:

(i) *Hysteresis and oscillatory behavior.* Razon and Schmitz (*4*) summarized the key experimental and modeling studies of steady-state multiplicity and intrinsic instabilities in platinum-catalyzed CO oxidation. Observations under UHV conditions of ignition–extinction phenomena (e.g., (*5–7*)), and of oscillations and travelling waves, have renewed interest in the many observations of these phenomena at higher pressures (e.g., (*13–21*)). Periodic behavior under UHV conditions has been observed for

* To whom correspondence should be addressed.

0021-9517/91 $3.00

the (100) and (110) planes of Pt (Ertl and co-workers (*8, 9, 22–24*)). LEED data confirms the oscillations are driven by a reversible reconstruction of the surface Pt atoms from the hex to (1 × 1) phase of Pt(100). Differences in heats of adsorption and sticking coefficients on the two surfaces provide a feedback mechanism for oscillation between the two Pt phases. In essence, the Pt(100) plane is two catalysts in one. Oscillations at higher pressure are attributed either to an oxidation–reduction mechanism (*16, 25, 19, 12, 4*), or to carbon formation (*21*). A key question is whether UHV and higher pressure multiplicity and oscillations have a common mechanistic origin. Specific differences in the multiplicity features are discussed below.

(ii) *Structure sensitivity.* Goodman and co-workers have demonstrated that CO oxidation is insensitive to changes in catalyst surface structure for Rh (*26*), Ru (*27*), and Pt, Pd, and Ir (*28*). These conclusions apply to the regime of a CO-covered surface. Similar conclusions were reached by McCarthy *et al.* (*29*) and Cant *et al.* (*30*).

(iii) *Bridging the gap between UHV and atmospheric pressure kinetic behavior of CO oxidation.* Many studies have shown that the rate of CO oxidation on noble metals is independent of total pressure for a CO-covered surface. The rate (r) in this regime is given by $r = k(T)p_{O_2}/p_{CO}$ with an apparent activation energy of about 30 kcal/mol (e.g., (*3, 28*)). These trends appear to be independent of the catalyst type and have been observed for a wide range of total pressures.

A similar consistency is not evident with regard to steady-state multiplicity and oscillatory rate features. These inconsistencies may be attributed to a difference in catalyst purity or to nonisothermal effects. While observations of oscillations on polycrystalline (supported or unsupported) catalysts are common at high pressure, no reports of periodic rates on polycrystalline Pt under UHV conditions have appeared. Indeed, oscillations under such clean conditions may only occur by a reconstruction mechanism.

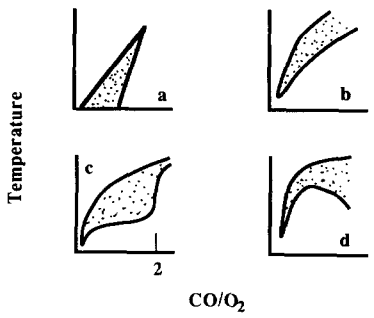

FIG. 1. Schematics of four different types of temperature–CO/O_2 bifurcation maps observed experimentally.

Berlowitz *et al.* (*28*) pointed out that clean Pt does not oxidize readily. This may explain the absence of oscillations in their Pt(100) study at intermediate pressure. Yeates *et al.* (*12*) suggested that reconstruction is unlikely at high pressures. On supported catalysts at high pressure, temperature nonuniformities are manifested as traveling waves and periodic rates (*20*).

The steady-state rate multiplicity features for CO oxidation are also different depending on the pressure and underlying mechanism, of which there are several. Multiple rate phenomena are qualitatively similar to oscillatory phenomena because of the existence of high and low rate regimes. If each branch is asymptotically stable, transitions between the states occur at ignition and extinction points as an operating parameter is slowly changed. For virtually all isothermal studies at any total pressure, the multivalued CO oxidation rate–CO pressure bifurcation diagram is in the form of a clockwise hysteresis loop (*4*). A bifurcation map shows the boundaries between the operating condition regions, such as in the catalyst temperature (T)–CO pressure (p_{CO}) plane, for which different numbers of steady-state rates are sustained for a fixed set of conditions (e.g., O_2 pressure). Although the bifurcation diagram pattern is consistent, the shape of the T–p_{CO} bifurcation map is not. Figure 1 is a schematic of the four types of temperature–CO pressure bifurcation maps

that have been experimentally observed for Pt-catalyzed CO oxidation. The temperature refers to the catalyst temperature for isothermal experiments (Figs. 1a–1c) and to the bulk gas temperature for the nonisothermal experiments (Fig. 1d). The oxygen pressure is fixed in these experiments. In all cases the ignition locus is to the left of the extinction locus. The enclosed portion shows the region in the (T–p_{CO}) plane giving two observed states for a fixed operating condition.

Map (a) is an inverted cusp that has been observed in two UHV studies: CO oxidation on polycrystalline Pt foil by Golchet and White (*5*) and on Pt (110) by Sung (*7*). (It should be pointed out that the hysteresis observed in the former study was not definite, due to the uncertain stability of the high rate state that overlapped with the low rate state for a large range of CO pressure.) The ignition and extinction temperatures are increasing functions of the CO pressure. For a sufficiently high temperature the rate is a single-valued function of the CO pressure. Since transport limitations are unlikely in a UHV experiment, one may infer that this multiplicity is of an intrinsic kinetic origin.

Map (b) is an upright cusp and has been observed at higher pressure, conditions for which mass transport limitations may exist. For example, Lindstrom and Tsotsis (*19*) reported this map for CO oxidation at intermediate total pressure (about 1 Torr) on a supported Pt wafer. We have obtained a similar map for CO oxidation on a Pt wire in our lab (*31, 1*). Graham and Lynch (*32*) observed this shape for atmospheric pressure CO oxidation on supported Pt.

Map (c) is a cusp with an added feature. The extinction locus displays a rather sharp transition at approximately the stoichiometric ratio, $p_{CO}/p_{O_2} = 2$. This feature was observed by Kaul and Wolf (*20*) and is inferred from the data of Haaland and Williams (*17*) for reaction at 1 atm on a wafer.

Map (d) has the added complexity of local extrema along the extinction branch. It was observed for nonisothermal atmospheric pressure CO oxidation on a Pt wire (*33*), on a single supported Pt pellet (*18, 34*), and on wafers (*35, 36*). The negative slope portion of the extinction branch is most likely a result of the classic thermokinetic interaction for exothermic catalytic reactions (*37, 34*).

The primary objective of this two-part study is to link the steady-state kinetics of Pt-catalyzed CO oxidation over a wide range of conditions. For example, one question to address is whether or not a single model can predict the apparently disparate isothermal bifurcation maps (Figs. 1a–1c) obtained over a wide range of pressures and for different types of Pt catalysts. We feel that it is essential to understand the causative mechanisms for the more basic kinetic and more complex multiplicity features before addressing dynamic behavior and oscillatory phenomena. Ertl and co-workers have predicted the trends in the oscillatory data obtained for Pt(100) with a sophisticated model that accounts for the quite different kinetics on the hex and (1×1) surface structures (e.g., (*22*)). However, necessarily different mechanism(s) cause the hysteresis for catalysts that are not apt to reconstruct (e.g., other planes), or reconstruct only on the exposed (100) (and possibly (110)) planes on the surface of foils, wires, and supported metals. Our analysis is limited to such Pt catalysts.

In this first part detailed analyses of the predicted kinetic and multiplicity features of several potential CO oxidation kinetic models are carried out. First we show that the basic three-step model is incapable of predicting the correct kinetic features in the limit of the oxygen- or CO-covered surfaces. Then four new models are developed that capably predict observed steady-state kinetic and multiplicity features. Singularity theory methods are used to delineate the observed multiplicity features of the multivalued kinetic models. Several of the modifications of the basic model have been offered previously. However, the key is that the new models can each satisfy the experimental kinetics and multiplicity constraints.

In the second part the robustness of the models are checked by simulating kinetic behavior over a total pressure range spanning UHV to atmospheric (*1*).

Model I: Basic Three-Step Sequence

Model Development

The oxidation of carbon monoxide on platinum is commonly postulated to proceed by the three-step sequence (*3, 4*):

$$\begin{aligned}&(1)\ CO + X \leftrightarrow CO\text{–}X\\ &(2)\ O_2 + 2X \leftrightarrow 2O\text{–}X\\ &(3)\ CO\text{–}X + O\text{–}X \rightarrow CO_2 + 2X \end{aligned} \quad (1)$$

This sequence has been used to explain the kinetics of CO oxidation (*38–42, 25, 12, 36*). Implicit in sequence (1) is the assumption that the catalytic site (X) is identical in each elementary step.

Several investigators have proposed the following bimolecular Langmuir–Hinshelwood rate expression to explain and/or fit data obtained for atmospheric pressure CO oxidation on various supported Pt catalysts (*43–47, 29, 34*):

$$\text{Rate} = \frac{k_{sr}K_{CO}K_{O_2}p_{CO}p_{O_2}}{(1 + K_{CO}p_{CO} + K_{O_2}p_{O_2})^2}. \quad (2)$$

Implicit in the derivation of (2) is a surface reaction (sr) controlled rate with CO and molecular oxygen coverages given by their equilibrium values. This model correctly predicts a rate that is proportional to $(p_{CO})^{-1}p_{O_2}$ for the CO-covered surface. While expression (2) may adequately fit the kinetic data or predict isothermal multiplicity when coupled with mass transport, it is known that (i) the surface reaction is not the single controlling step, and thus adsorption equilibrium for CO and O_2 is not attained under most conditions, (ii) dissociative oxygen adsorption is the dominant mechanism for a surface not covered with CO, and (iii) oxygen desorption is negligible for temperatures less than 700 K (*3*). Moreover, the model cannot predict intrinsic rate multiplicity.

Our goals in this section are to show that the three-step model capably predicts the (T, p_{CO}) inverted cusp (Fig. 1a), to demonstrate the limitations of the model in predicting the proper reaction orders and apparent activation energy, and to illustrate the utility of singularity theory in the analysis.

The model consists of coverage balances for CO and oxygen, and an overall site balance,

$$k_1p_{CO}\theta_v - k_{-1}\theta_{CO} - k_3\theta_{CO}\theta_O = 0 \quad (3)$$

$$2k_2p_{O_2}\theta_v^2 - 2k_{-2}\theta_O^2 - k_3\theta_{CO}\theta_O = 0 \quad (4)$$

$$\theta_{CO} + \theta_O + \theta_v = 1, \quad (5)$$

where v denotes vacant. The adsorption constants are given by

$$k_1 = \sqrt{\frac{1}{2\pi M_{CO}RT_b}}S_{CO} \quad (6)$$

$$k_2 = \sqrt{\frac{1}{2\pi M_{O_2}RT_b}}S_O, \quad (7)$$

where S_i is the initial sticking coefficient for species i, M_i is molecular weight of species i, R is the gas constant, and T_b is the bulk gas temperature. The remaining constants are assumed to depend only on the catalyst temperature T according to

$$k_i = k_i(T_r)\exp\left\{\frac{E_i}{RT_r}\left(1 - \frac{T_r}{T}\right)\right\}; \quad i \equiv -1, -2, 3, \quad (8)$$

where T_r is a reference temperature and E_i is activation energy. Equations (3), (4), and (5) are nondimensionalized and combined to give an implicit function of the single state variable θ_{CO}:

$$\begin{aligned}F(\theta_{CO}, \mathbf{p}) = {}& \gamma[(\beta + \alpha\theta_{CO})(1 - \theta_{CO})\\ &- (\beta(1 - \theta_{CO}) - \theta_{CO})]^2\\ &- \phi[\beta(1 - \theta_{CO}) - \theta_{CO}]^2\\ &- (\beta + \alpha\theta_{CO})\theta_{CO}(\beta(1 - \theta_{CO})\\ &- \theta_{CO}) = 0, \end{aligned} \quad (9)$$

where $\mathbf{p}$ is a vector of model parameters (α, β, γ, ϕ). These parameters are functions

of the dimensionless temperature $y(=T/T_r)$ according to

$$\alpha = \alpha_r X_\alpha(y) \quad \beta = \beta_r X_\beta(y)$$
$$\gamma = \gamma_r X_\gamma(y) \quad \phi = \phi_r X_\phi(y), \qquad (10)$$

where $X_j(y) = \exp\{E_j(1 - 1/y)\}(j \equiv \alpha, \beta, \gamma, \phi)$, and the subscript r denotes evaluation at reference temperature T_r. The parameters are defined as

$$\alpha_r = \frac{k_3(T_r)}{k_{-1}(T_r)} \qquad \beta_r = \frac{k_1 p_{CO}}{k_{-1}(T_r)}$$
$$\gamma_r = \frac{2k_2 p_{O_2}}{k_3(T_r)} \qquad \phi_r = \frac{2k_{-2}(T_r)}{k_3(T_r)}$$
$$E_\alpha = \frac{E_3 - E_{-1}}{RT_r} \qquad E_\beta = -\frac{E_{-1}}{RT_r}$$
$$E_\gamma = -\frac{E_3}{RT_r} \qquad E_\phi = \frac{E_{-2} - E_3}{RT_r}. \qquad (11)$$

The atomic oxygen coverage depends on θ_{CO} according to

$$\theta_O = \frac{\beta(1 - \theta_{CO}) - \theta_{CO}}{\beta + \alpha\theta_{CO}}. \qquad (12)$$

Algebraic manipulations of $F(\theta_{CO}) = 0$ (Eq. (9)) give

$$F(\theta_{CO}, \mathbf{p}) = \theta_{CO}^4[\alpha^2\gamma] + \theta_{CO}^3[\alpha(\beta + 1) - 2\alpha\gamma(\alpha + 1)] + \theta_{CO}^2[\gamma(\alpha + 1)^2 + \beta(\beta + 1 - \alpha) - \phi(\beta + 1)^2] + \theta_{CO}[-\beta(\beta - 2\phi(\beta + 1))] - \phi\beta^2 = 0 \qquad (13)$$

which is a fourth-order polynomial in θ_{CO}. Calculation of the rate requires the solution first of Eq. (13) for θ_{CO} and then Eq. (12) for θ_O, for a specified operating condition (i.e., values of $\alpha, \beta, \gamma, \phi$). The dimensionless rate (r_D) is given by

$$r_D = \theta_{CO}\theta_O. \qquad (14)$$

Multiplicity Analysis

It first is of interest to determine if this basic model I predicts the qualitative trends in rate multiplicity data obtained under UHV conditions. The reader is referred to the works of Balakotaiah and Luss (*48, 49*) and Golubitsky and Schaeffer (*50*) for detailed presentation of the singularity theory which we apply in the analysis below.

For a single-state variable function $F(\theta_{CO}, \mathbf{p}) = 0$, the ignition and extinction loci satisfy the defining conditions

$$F(\theta_{CO}, \mathbf{p}) = \frac{dF}{d\theta_{CO}} = 0. \qquad (15)$$

A bifurcation map is constructed by solving (15). The point at which the ignition and extinction loci coalesce is a cusp point, which satisfies the defining conditions

$$F(\theta_{CO}, \mathbf{p}) = \frac{dF}{d\theta_{CO}} = \frac{d^2F}{d\theta_{CO}^2} = 0. \qquad (16)$$

The locus of cusp points is called the hysteresis variety. An extremum point with respect to a parameter in a bifurcation map (e.g., Fig. 1d) is an isola point, which satisfies the conditions

$$F(\theta_{CO}, \mathbf{p}) = \frac{\partial F}{\partial\theta_{CO}} = \frac{\partial F}{\partial\lambda} = 0, \qquad (17)$$

where λ is the bifurcation parameter. The locus of isola points is called the isola variety.

The basic model predicts up to three feasible solutions (i.e., $0 \le \theta_{CO}, \theta_O \le 1$) for feasible parameter values ($\alpha, \beta, \gamma, \phi > 0$). Figure 2 shows three γ–β bifurcation maps corre-

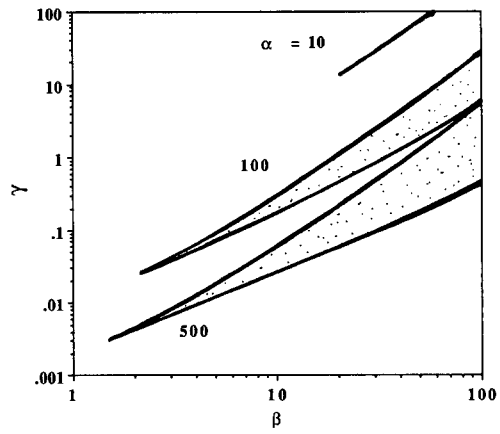

FIG. 2. Cross sections of bifurcation set for the three-step model plotted in the plane of $\gamma (= 2k_2 p_{O_2}/k_3)$ – $\beta (= k_1 p_{CO}/k_{-1})$ for different values of $\alpha (= k_3/k_{-1})$.

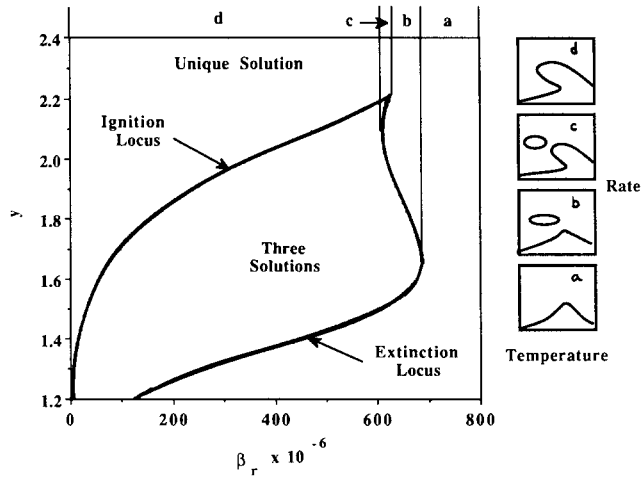

FIG. 3. Dimensionless temperature ($y = T/T_r$) versus dimensionless CO pressure ($\beta_r = k_1 p_{CO}/k_{-1}(T_r)$) bifurcation map. Also provided are schematics of the dimensionless rate ($\theta_{CO}\theta_{CO}$) versus dimensionless temperature (y) bifurcation diagrams for four different β_r values. The diagram types (a)–(d) are obtained by fixing β_r within the ranges (a)–(d) shown. Parameter values provided in Table 1.

sponding to $\alpha = 10$, 100, and 500, with $\phi = 0$ (no oxygen desorption), and $y = 1$ ($T = T_r$; i.e., $\gamma = \gamma_r$, $\beta = \beta_r$, $\alpha = \alpha_r$). These were constructed by applying (15) (details in Appendix B). The γ–β map can be interpreted as a constant temperature, p_{O_2}–p_{CO} map. Each map has the shape of an upright cusp. The multivalued rate–γ bifurcation diagram for fixed β is in the form of a counterclockwise hysteresis loop, while the rate versus β diagram for fixed γ is a clockwise hysteresis loop. As α increases the cusp point moves to lower γ and β and the multiplicity region expands. It can be shown that for sufficiently small α multiplicity is not encountered for any γ or β values. These features are consistent with UHV data (e.g., (7)). For a fixed catalyst temperature, an increase in oxygen pressure expands the range of CO pressures for which two states are observed. The predictions also underscore the fact that for a sufficiently slow surface reaction step (i.e., α) the rate is single-valued (i.e., see Eq. (2)).

Model I predicts some intriguing multiplicity features for cases in which the catalyst temperature is a parameter. This is due in part to the exponential temperature dependence of the desorption and surface reaction rate constants. A typical y–β_r ($= k_1 p_{CO}/k_{-1}(T_r)$) bifurcation map is shown in Fig. 3. It can be viewed as a catalyst temperature–CO pressure map, as in Fig. 1. The remaining parameter values are provided in Table 1. These values reasonably represent CO oxidation without transport limitations: (i) a reaction step that is much faster than CO desorption ($\alpha_r = 10^5$), (ii) CO desorption activation energy of about 30 kcal/mol ($E_\beta = -30$, with $T_r \approx 400$ K), (iii) a slightly lower surface reaction activation energy ($E_\gamma = -25$), and (iv) a highly activated oxygen desorption step ($\phi_r = 10^{-4}$, $E_\phi = 30$). The map has the local inverted cusp character (as in Fig. 1a) with the additional features of two extremum points with respect to y along the extinction locus.

TABLE 1

Parameter Values Used for Construction of Bifurcation Map and Diagrams in Figs. 4 and 5

$\alpha_r = 10^5$	$E_\alpha = -5$
$\gamma_r = 10^5$	$E_\gamma = -25$
$\phi_r = 10^{-4}$	$E_\phi = 30$
	$E_\beta = -30$

Quite interesting bifurcation diagrams are predicted if the CO pressure (β_r) is fixed and the temperature (y) is varied, as depicted schematically in Fig. 3. A single-valued diagram (a) is obtained for β_r values to the right of the β_r value corresponding to the lower temperature isola point, $\beta_{r,I1}$. A closed isola appears for β_r between $\beta_{r,I1}$ and $\beta_{r,C}$, the β_r value corresponding to the cusp (diagram (b)). As β_r is decreased below $\beta_{r,C}$ the lower rate branch exhibits a counterclockwise hysteresis loop for a small y range. For $\beta_{r,I2} < \beta_r < \beta_{r,C}$ diagram (c) is obtained which has a 1–3–1–3–1 multiplicity pattern. Finally, as β_r is decreased below $\beta_{r,I2}$ the higher y extinction point of the isola and the extinction point belonging to the hysteresis loop coalesce, giving diagram (d).

An obvious and important question is whether such bifurcation features may be observed experimentally. To answer this question, it would help to know the range of operating conditions in which different types of rate versus temperature bifurcation diagrams are encountered. It would be even more helpful to know when to expect a certain type of temperature–CO pressure bifurcation map.

The first task involves the division of parameter space into regions in which different types of CO coverage (or, equivalently, rate)–temperature (y) bifurcation diagrams are encountered. This involves the construction of the hysteresis and isola varieties (*48, 49*). The hysteresis (H) variety for the single-state variable function $F(\theta_{CO}, y, \mathbf{p}) = 0$ satisfies (16) and the nondegeneracy conditions

$$\frac{\partial F}{\partial y}\frac{\partial^3 F}{\partial \theta_{CO}^3} \neq 0.$$

When crossing this variety two limit points appear (or disappear) in the θ_{CO} (or rate) versus y bifurcation diagram in the form of a hysteresis loop. Computation of the H variety for the three-step model is described in Appendix A. The isola (I) variety satisfies the defining conditions in (17). When crossing this variety two limit points appear or disappear and either the bifurcation diagram separates into two isolated curves if

$$Q \equiv \frac{\partial^2 F}{\partial \theta_{CO} \partial y} - \frac{\partial^2 F}{\partial \theta_{CO}^2}\frac{\partial^2 F}{\partial y^2} > 0$$

or an isolated branch of solutions appears if $Q < 0$.

One may calculate the H and I varieties in order to locate the regions in parameter space within which qualitatively different rate ($\theta_{CO}\theta_O$)–temperature (y) diagrams are encountered. Such a "map" of bifurcation diagrams enables one to bound, say, the oxygen and CO pressures for which a particular bifurcation diagram is obtained (see (*51*) for details). A series of such maps may be useful for estimating kinetic parameters based on an analysis of bifurcation diagram type.

A more revealing but difficult task is to divide the parameter space into regions in which different types of temperature (y)–CO pressure (β_r) bifurcation maps exist. Our approach involves the computation of singular points that are encountered when the qualitative features of a map change. Harold *et al.* (*37*) analyzed a simpler model using a less general technique.

Figure 4 shows examples of four types of transitions that account for changes in the

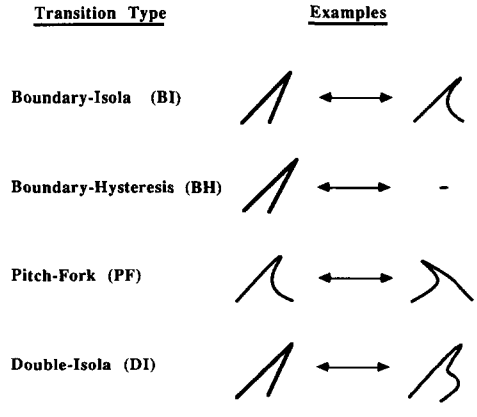

FIG. 4. Schematic of the four types of transitions that account for changes in the qualitative features of temperature–CO pressure bifurcation maps.

y–β_r map features. The map features are determined by the number and relative location of cusp and isola points within a specified feasible operating boundary. We specify *a priori* that this boundary is given by $y > y_l$, where y_l is the lowest temperature admitted, and $\beta_r > 0$. Our analysis is simplified somewhat because no isola points with respect to β_r are predicted for physically realizable parameter values.

The first transition is the intersection of an isola point with the boundary $y = y_l$. We refer to this as the boundary–isola (BI) transition. As the parameters cross the BI transition an isola point appears or disappears along the ignition or extinction locus. The defining conditions are

$$\text{BI: } F = \frac{\partial F}{\partial \theta_{CO}} = \frac{\partial F}{\partial y} = 0, \quad y = y_l \quad (18)$$

with the nondegeneracy conditions

$$\text{BI: } \det(d^2F) \neq 0, \quad y = y_l,$$

where

$$\det(d^2F) = \frac{\partial^2 F}{\partial \theta_{CO}^2}\frac{\partial^2 F}{\partial y^2} - \left(\frac{\partial^2 F}{\partial \theta_{CO}\partial y}\right)^2. \quad (19)$$

An example is the appearance of an isola along the extinction branch of an inverted cusp (Fig. 4).

The second transition is the intersection of a cusp point with the boundary $y = y_l$, the boundary–hysteresis (BH) transition. As the parameter set crosses this transition a cusp point appears or disappears. The defining conditions are

$$\text{BH: } F = \frac{\partial F}{\partial \theta_{CO}} = \frac{\partial^2 F}{\partial \theta_{CO}^2} = 0, \quad y = y_l \quad (20)$$

with the nondegeneracy conditions

$$\text{BH: } \frac{\partial F}{\partial y} \neq 0, \quad \frac{\partial^3 F}{\partial \theta_{CO}^3} \neq 0. \quad (21)$$

An example is the disappearance of an inverted cusp from the (y, β_r) feasible domain (Fig. 4).

The third transition is the intersection of the hysteresis and cusp varieties, which is called a pitchfork point. This pitchfork (PF) transition appears in the (y, β_r) map as the coalescence of a cusp point with a local extremum (isola point). The defining conditions are

$$\text{PF: } F = \frac{\partial F}{\partial \theta_{CO}} = \frac{\partial^2 F}{\partial \theta_{CO}^2} = \frac{\partial F}{\partial y} = 0 \quad (22)$$

with the nondegeneracy conditions

$$\text{PF: } \frac{\partial^3 F}{\partial \theta_{CO}^3} \neq 0, \quad \frac{\partial^2 F}{\partial \theta_{CO}\partial y} \neq 0, \quad \frac{\partial^2 F}{\partial y^2} \neq 0. \quad (23)$$

An example is the movement of an isola point from the extinction to the ignition branch (Fig. 4).

The fourth transition is the coalescence of two isola points, which we refer to as a double-isola (DI) transition. As the parameter set crosses this transition two isola points appear or disappear along the ignition or extinction locus. The defining conditions are

$$\text{DI: } F = \frac{\partial F}{\partial \theta_{CO}} = \frac{\partial F}{\partial y} = \det(d^2F) = 0 \quad (24)$$

with the nondegeneracy conditions

$$\text{DI: } \frac{\partial^2 F}{\partial \theta_{CO}^2} \neq 0, \quad \frac{\partial^2 F}{\partial \theta_{CO}\partial y} \neq 0. \quad (25)$$

An example is a shift from an inverted cusp to one with two extrema along the extinction locus (Fig. 4).

This approach of dividing the parameter space into different types of (y, β_r) maps is now illustrated for the three-step CO oxidation model (Eq. (13)). Appendix B provides the equations and solution strategies used. In our sample calculation, ϕ_r, α_r and the dimensionless activation energies (E_i's) are fixed at the values shown in Table 1, and the lower temperature bound is assigned as unity ($y_l = 1$). The computed transitions are plotted in the (ϕ_r, γ_r) plane (Fig. 5). Figure 5 can be interpreted as the plane of oxygen desorption rate versus oxygen adsorption rate. The plane is divided into four regions (1–4) within each of which a different type of temperature–CO pressure (y, β_r) map is

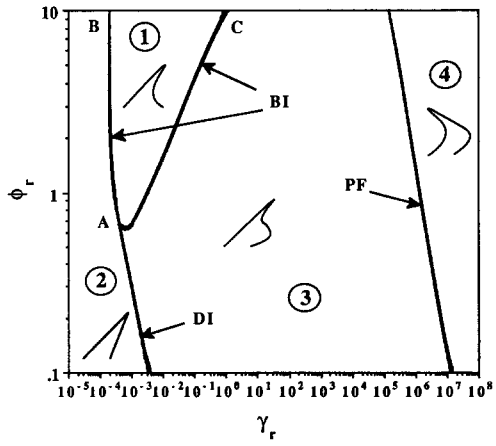

FIG. 5. Division of the (ϕ_r, γ_r) plane into regions containing different types of y–β_r bifurcation maps.

obtained. The BI transition has a parabolic shape with a local minimum. The BH transition does not exist for this choice of parameters. The PF transition is a negatively sloped curve at high γ_r values. The DI transition intersects the BI transition at point A. Within region 1 (formed by the BI transition) the map with a single isola point along the extinction locus exists. This map shifts either to (i) the inverted cusp upon crossing the BI transition locus between points A and B into region 2, or (ii) a map with two isola points along the extinction locus upon crossing the BI transition locus between points A and C into region 3. Finally, to the right of the PF transition locus is region 4 within which the map has isola points along the ignition and extinction loci.

Figure 5 reveals that for sufficiently low oxygen adsorption rates (low γ_r values) the experimentally observed cusp is predicted. This γ_r value range expands as the oxygen desorption rate (ϕ_r) decreases. Thus, a decreasing rate of oxygen desorption (ϕ_r) increases the range of oxygen pressures (γ_r) for which the inverted cusp temperature–p_{CO} map is obtained. In fact, typical estimated values of ϕ_r and γ_r from UHV experiments fall well within region 2. This is evidence that the inverted cusp shape of the T–p_{CO} map is the expected shape resulting from the inherent nonlinearities of the basic three-step model.

Kinetic Analysis

Although the well-accepted three-step model capably predicts the multiplicity features of UHV CO oxidation data, the same is not true for some of the basic kinetic features. Consider the regime of CO inhibition, within which the experimental rate follows the expression $k(T)p_{O_2}/p_{CO}$ with an apparent activation energy of about 30 kcal/mol. If we demand that the atomic oxygen coverage is quite small ($\theta_O \to 0$) and oxygen desorption is neglected ($k_{-2} = 0$), which is a good assumption below 700 K (*3*), Eqs. (3) and (4) are combined to give the following quadratic function of θ_{CO}:

$$\alpha\gamma\theta_{CO}^2 + (\beta + 1 - 2\alpha\gamma)\theta_{CO} + \alpha\gamma - \beta = 0. \quad (26)$$

The feasible solution of (26) together with the rate expression

$$\text{Rate} = k_3(T)\theta_{CO}\theta_O = k_3(T)[\beta(1 - \theta_{CO}) - \theta_{CO}]/\alpha \quad (27)$$

describes the CO inhibition kinetic regime. The apparent activation energy (E_a) is given by

$$E_a = -R\left\{\frac{d\ln(\text{Rate})}{d(1/T)}\right\}, \quad (28)$$

which in dimensionless form is

$$\varepsilon_a = \varepsilon_3 - \frac{d(\ln r_D)}{d(1/y)}, \quad (29)$$

where

$$\varepsilon_a = \frac{E_a}{RT_r} \quad \varepsilon_3 = \frac{E_3}{RT_r} \quad r_D = \theta_{CO}\theta_O \quad (30)$$

(see Appendix C for the details in applying (29) to the model Eqs. (26), (27)). The result is:

$$\varepsilon_a = \left(\frac{2}{1 - \theta_{CO}}\right)\frac{d\theta_{CO}}{d(1/y)}, \quad (31)$$

where θ_{CO} is the feasible solution of (26),

$$\theta_{CO} = -\frac{\beta + 1 - 2\alpha\gamma}{2\alpha\gamma} \pm \frac{\sqrt{\Delta}}{2\alpha\gamma};$$
$$\Delta = (\beta + 1 - 2\alpha\gamma)^2 - 4\alpha\gamma(\alpha\gamma - \beta) \quad (32)$$

and where

$$\frac{d\theta_{CO}}{d(1/y)} = -\frac{1}{2\alpha\gamma}\left\{-E_\beta\beta \mp \frac{1}{2\sqrt{\Delta}}\frac{d(\Delta(y))}{d(1/y)} + (E_\alpha + E_\gamma)(\beta + 1 \mp \sqrt{\Delta})\right\}. \quad (33)$$

The derivative $d(\Delta(y))/d(1/y)$ is provided in Appendix C.

Examination of the apparent activation energy ε_a (Eqs. (31)–(33)) reveals three key points. First, the rate depends on y, β_r, E_β, the product $\alpha_r\gamma_r$ ($=2k_2p_{O_2}/k_{-1}(T_r)$), and the sum $E_\alpha + E_\gamma (= -\varepsilon_{-1} = -E_{-1}/RT_r)$. Thus, the desorption of CO and adsorption of O_2 are the only potential rate-limiting steps in this regime. Second, it is easily shown that for decreasing temperature (y) the apparent activation energy approaches a value that is twice the CO desorption activation energy (see (*51*)). Third, as $\alpha_r\gamma_r \to 0$, oxygen adsorption becomes limiting and the CO coverage approaches its equilibrium value. In this regime it is easily shown that the apparent activation energy is given by

$$\varepsilon_a(\alpha_r\gamma_r \to 0) = -\frac{2\beta E_\beta}{1 + \beta}. \quad (34)$$

Equation (34) predicts that for low temperature $\varepsilon_a \to -2E_\beta = 2\varepsilon_{-1}$. Moreover, the rate is given by

$$\text{Rate} = \frac{k_2 p_{O_2}}{\left(1 + \frac{k_1 p_{CO}}{k_{-1}}\right)^2}. \quad (35)$$

Equation (35) predicts a rate which is first order in oxygen but (−2) order in the CO pressure.

Thus, the three-step model fails to predict the correct temperature dependence or reaction order with respect to CO for the CO adsorption inhibited regime. The predicted apparent activation energy and order with respect to CO are twice the values observed experimentally. This factor of two is directly linked to the three-step model requirement that the oxygen adsorb dissociatively on two vacant sites even when there are few vacant sites available. Below we show that model I also fails to predict the first-order CO dependence when the surface is covered with oxygen. Moreover, it can be shown that the rate is inhibited by oxygen. These predictions are contrary to experimental observation.

DEVELOPMENT AND ANALYSIS OF FOUR NEW MODELS

In this section four new models are developed. Our approach is to add features to the model I framework in order to correct the limiting-regime kinetic predictions but to retain the correct multiplicity feature predictions.

Model II: Molecularly Adsorbed Oxygen and Eley–Rideal Reactions

Model Development

In this model the following five steps are postulated to occur in addition to steps (1)–(3) (in Eq. (1)):

$$(4): O_2 + X \leftrightarrow O_2\text{–}X$$
$$(5): O_2\text{–}X + X \to 2O\text{–}X$$
$$(6): 2CO\text{–}X + O_2\text{–}X \to 3X + 2CO_2$$
$$(7): CO + O\text{–}X \to CO_2 + X$$
$$(8): CO + O_2\text{–}X \to CO_2 + O\text{–}X. \quad (36)$$

The two new features of this eight-step model are (i) adsorbed molecular oxygen participates in the sequence (steps (4)–(6) and (8)), and (ii) two reactions involving gas phase CO and adsorbed oxygen species (steps (7) and (8)) augment the Langmuir reaction steps (3) and (6).

Regarding new feature (i), previous investigators have proposed steps (4) and (6) for CO oxidation (e.g., (*52, 30*)). Monroe and Merrill (*53*) showed that oxygen adsorption on Pt(111) requires a single site. Langmuir (*54*) and Oh *et al.* (*26*) inferred that the ap-

parent activation in the CO adsorption inhibited regime is equal to the CO binding energy only if oxygen requires a single site for adsorption. Model II assumes that oxygen can adsorb both by the conventional, direct dissociative step (2) and by a two-step ((4) and (5)) molecular precursor mechanism. Moreover, both oxygen adsorption steps (2) and (4) are assumed irreversible. The step (2) irreversibility is expected under 700 K. The step (4) irreversibility follows from an anticipated rapid consumption of adsorbed molecular oxygen by irreversible dissociation (step (5)) or reaction (steps (6) and (8)). A motivation for the dual adsorption pathways is that the existence of multiple solutions requires the second-order dissociative adsorption step (2) if step (4) is irreversible. The key to steps (4)–(6) is that on a CO-covered surface with few available empty sites molecular oxygen adsorption (step (4)) dominates. A lack of vacant sites inhibits direct dissociative adsorption (step (2)) or molecular oxygen dissociation (step (5)). In model V described below oxygen is permitted to adsorb only by step (4), which is assumed to be at equilibrium. Also, reaction between adsorbed CO and molecular oxygen is assumed bimolecular rather than termolecular. As shown below, these subtle differences between models II and V affect the predicted kinetic behavior.

The reaction steps (7) and (8) are proposed as additional channels for the production of CO_2. Step (7) has been used by several investigators to explain the observation that CO reacts readily with an oxygen-covered surface (*55–57, 22*). An elementary Eley–Rideal (ER) reaction between gaseous CO and adsorbed oxygen has fallen out of favor for Pd because of UHV evidence (*3*). However, there is debate about the existence of an ER-like reaction for the oxygen-covered Pt surface, especially for higher pressures. In proposing steps (7) and (8) we make no assumptions with respect to specific reaction intermediates or to the dynamics of the steps. Indeed, the steps are not necessarily elementary. The motivation is from the kinetics; our analysis below indicates the inclusion of steps (7) and (8) gives a predicted rate which is temperature insensitive and first order in CO for a gas phase containing a low CO/O_2 ratio. This agrees with most observations.

The CO, atomic and molecular oxygen, and overall site balances are respectively given by

$$\beta\theta_{v,CO} - \theta_{CO} - \alpha\theta_{CO}\theta_O - 2\eta\alpha\theta_{CO}^2\theta_{O_2} = 0 \tag{37}$$

$$\gamma\theta_{v,O}^2 - \theta_{CO}\theta_O + 2\delta\theta_{O_2}\theta_{v,O} - \frac{\beta\xi}{\alpha}\theta_O + \frac{\beta\kappa}{\alpha}\theta_{O_2} = 0 \tag{38}$$

$$\Gamma\theta_{v,O} - \eta\theta_{CO}^2\theta_{O_2} - \delta\theta_{O_2}\theta_{v,O} - \frac{\beta\kappa}{\alpha}\theta_{O_2} = 0 \tag{39}$$

$$\theta_{CO} + \theta_O + \theta_{O_2} + \theta_{v,CO} = 1 \tag{40.a}$$

$$e\theta_{CO} + f\theta_O + f\theta_{O_2} + \theta_{v,O} = 1. \tag{40.b}$$

Again, desorption of atomic and molecular oxygen and surface reconstruction are neglected in Eqs. (37) and (40). Note that a distinction is made in the equations between the fraction of vacant sites available for CO adsorption ($\theta_{v,CO}$) and for the atomic and molecular oxygen ($\theta_{v,O}$). The parameters e and f are defined for model III below. For model II, e and f are equal to unity, and thus $\theta_{v,CO} = \theta_{v,O}$. Model II reduces to the three-step model I by letting $\Gamma \to 0$.

Three new parameters η, δ, and Γ are defined at the reference temperature T_r as

$$\eta_r = \frac{k_6(T_r)}{k_3(T_r)} \quad \delta_r = \frac{k_5(T_r)}{k_3(T_r)} \quad \Gamma_r = \frac{k_4 p_{O_2}}{k_3(T_r)}. \tag{41}$$

For any temperature (y) we have

$$\eta = \eta_r X_\eta(y) \quad \delta = \delta_r X_\delta(y) \quad \Gamma = \Gamma_r X_\Gamma(y), \tag{42}$$

where $X_j(y) = \exp\{E_j(1 - 1/y)\}$ ($j \equiv \eta, \delta, \Gamma$), and where

$$E_\eta = \frac{E_6 - E_3}{RT_r} \quad E_\delta = \frac{E_5 - E_3}{RT_r} \quad E_\Gamma = -\frac{E_3}{RT_r}. \tag{43}$$

The molecular oxygen adsorption constant, k_4, is given by an expression similar to Eq. (7). Two other temperature independent parameters ξ and κ are the ratios:

$$\xi = \frac{k_7}{k_1} \quad \kappa = \frac{k_8}{k_1}. \tag{44}$$

Equations (37)–(40) can be simplified as follows. θ_{O_2} appears linearly in Eq. (37), giving

$$\theta_{O_2} = \frac{\beta(1 - \theta_{CO} - \theta_O) - \theta_{CO} - \alpha\theta_{CO}\theta_O}{\beta + 2\eta\alpha\theta_{CO}^2}. \tag{45}$$

Substitution of (45) into (38) and (39) gives two nonlinear functions of θ_{CO} and θ_O,

$$G_1(\theta_{CO}, \theta_O, \mathbf{p}) = f_{11}(\theta_{CO})\theta_O^2 + f_{12}(\theta_{CO})\theta_O + f_{13}(\theta_{CO}) = 0 \tag{46}$$

$$G_2(\theta_{CO}, \theta_O, \mathbf{p}) = f_{21}(\theta_{CO})\theta_O^2 + f_{22}(\theta_{CO})\theta_O + f_{23}(\theta_{CO}) = 0, \tag{47}$$

where the coefficients $f_{ij}(\theta_{CO})$ are given by the rather cumbersome expressions (49a)–(49f) in Table 2. The rate is given by

$$\text{Rate} = k_3(T)\theta_{CO}\theta_O + 2k_6(T)\theta_{CO}^2\theta_{O_2} + k_7 p_{CO}\theta_O + k_8 p_{CO}\theta_{O_2}. \tag{48}$$

It is convenient to reduce the two nonlinear equations (46) and (47) in two state variables to a single equation in one intrinsic state variable. The key advantage of the single equation is that the various singular point defining conditions for a single variable function provided earlier can be used directly. This step follows a procedure involving the reduction of an arbitrary number of polynomial equations to a single one (*58*). Appendix D highlights the steps in obtaining the single function of θ_{CO} given by

$$F(\theta_{CO}, \mathbf{p}) \equiv (f_{21}f_{13} - f_{11}f_{23})^2 - (f_{23}f_{12} - f_{13}f_{22})(f_{11}f_{22} - f_{21}f_{12}) = 0, \tag{50}$$

where $f_{ij}(i, j = 1, 2, 3)$ are defined in Table 2 and $\mathbf{p}$ is a vector of parameters. For a given set of parameters Eq. (50) is solved for θ_{CO}. θ_O is given by

$$\theta_O = \frac{f_{21}f_{13} - f_{11}f_{23}}{f_{11}f_{22} - f_{21}f_{12}} \tag{51}$$

and θ_{O_2} by Eq. (45).

TABLE 2

Expressions for Coefficients Appearing in Eqs. (46) and (47)

$$f_{11}(\theta_{CO}) = \gamma[f^2(\beta + 2\eta\alpha\theta_{CO}^2)(\beta + 2\eta\alpha\theta_{CO}^2 - 2(\beta + \alpha\theta_{CO})) + (\beta + \alpha\theta_{CO})^2] + 2\delta\alpha f(\beta + \alpha\theta_{CO})(2\eta\theta_{CO} - 1)\theta_{CO} \tag{49a}$$

$$f_{12}(\theta_{CO}) = 2\gamma[-(\beta + 2\eta\alpha\theta_{CO}^2)^2(1 - \theta_{CO})f + (\beta(1 - \theta_{CO}) - \theta_{CO})[(\beta + 2\eta\alpha\theta_{CO}^2)f^2 - (\beta + \alpha\theta_{CO})] + f(\beta + 2\eta\alpha\theta_{CO}^2)(1 - \theta_{CO})(\beta + \alpha\theta_{CO})] - (\beta + 2\eta\alpha\theta_{CO}^2)^2\theta_{CO} + 2\delta[-(\beta + 2\eta\alpha\theta_{CO}^2)((\beta + \alpha\theta_{CO})(1 - \theta_{CO}) + f(\beta(1 - \theta_{CO}) - \theta_{CO})) + 2f(\beta + \alpha\theta_{CO})(\beta(1 - \theta_{CO}) - \theta_{CO})] - \beta\xi(\beta + 2\eta\alpha\theta_{CO}^2)^2/\alpha - \beta\kappa(\beta + 2\eta\alpha\theta_{CO}^2)(\beta + \alpha\theta_{CO})/\alpha \tag{49b}$$

$$f_{13}(\theta_{CO}) = \gamma[(\beta + 2\eta\alpha\theta_{CO}^2)(1 - \theta_{CO})[(\beta + 2\eta\alpha\theta_{CO}^2)(1 - \theta_{CO}) - 2f(\beta(1 - \theta_{CO}) - \theta_{CO})] + (\beta(1 - \theta_{CO}) - \theta_{CO})^2] + 2\delta(\beta(1 - \theta_{CO}) - \theta_{CO})[(\beta + 2\eta\alpha\theta_{CO}^2)(1 - \theta_{CO}) - f(\beta(1 - \theta_{CO}) - \theta_{CO})] + \beta\kappa(\beta + 2\eta\alpha\theta_{CO}^2)(\beta(1 - \theta_{CO}) - \theta_{CO})/\alpha \tag{49c}$$

$$f_{21}(\theta_{CO}) = -f\delta\alpha\theta_{CO}(\beta + \alpha\theta_{CO})(2\eta\theta_{CO} - 1) \tag{49d}$$

$$f_{22}(\theta_{CO}) = -f\Gamma\alpha\theta_{CO}(\beta + 2\eta\alpha\theta_{CO}^2)(2\eta\theta_{CO} - 1) + \eta\theta_{CO}^2(\beta + 2\eta\alpha\theta_{CO}^2)(\beta + \alpha\theta_{CO}) + \delta[(\beta + \alpha\theta_{CO})((\beta + 2\eta\alpha\theta_{CO}^2)(1 - \theta_{CO}) - f(\beta(1 - \theta_{CO}) - \theta_{CO})) + \alpha f\theta_{CO}(\beta(1 - \theta_{CO}) - \theta_{CO})(2\eta\theta_{CO} - 1)] + \beta\kappa(\beta + 2\eta\alpha\theta_{CO}^2)(\beta + \alpha\theta_{CO})/\alpha \tag{49e}$$

$$f_{23}(\theta_{CO}) = \Gamma(\beta + 2\eta\alpha\theta_{CO}^2)[(\beta + 2\eta\alpha\theta_{CO}^2)(1 - \theta_{CO}) - f(\beta(1 - \theta_{CO}) - \theta_{CO})] - \eta\theta_{CO}^2(\beta + 2\eta\alpha\theta_{CO}^2)(\beta(1 - \theta_{CO}) - \theta_{CO}) - \delta(\beta(1 - \theta_{CO}) - \theta_{CO})[(\beta + 2\eta\alpha\theta_{CO}^2)(1 - \theta_{CO}) - f(\beta(1 - \theta_{CO}) - \theta_{CO})] - \beta\kappa f(\beta(1 - \theta_{CO}) - \theta_{CO})(\beta + 2\eta\alpha\theta_{CO}^2)/\alpha \tag{49f}$$

Kinetic Analysis

It is revealing to analyze the kinetic behavior of a limiting case of model II. Suppose the sequence consists only of steps (1) (reversible CO adsorption), (4) (irreversible molecular oxygen adsorption), and (6) (termolecular reaction). In addition, suppose the coverage of molecular oxygen is very small ($\theta_{O_2} \to 0$). The dimensionless CO and O_2 balances are then given by

$$\beta(1 - \theta_{CO}) - \theta_{CO} - 2\alpha\eta\theta_{CO}^2\theta_{O_2} = 0 \quad (52)$$

$$\Gamma(1 - \theta_{CO}) - \eta\theta_{CO}^2\theta_{O_2} = 0. \quad (53)$$

Equations (52) and (53) are solved for θ_{CO} to give

$$\theta_{CO} = \frac{\beta - 2\alpha\Gamma}{\beta + 1 - 2\alpha\Gamma}. \quad (54)$$

A feasible solution requires that $\beta > 2\alpha\Gamma$. The rate is given by

$$\text{Rate} = \frac{2k_4p_{O_2}}{\dfrac{k_1p_{CO}}{k_{-1}} + 1 - \dfrac{2k_4p_{O_2}}{k_{-1}}}. \quad (55)$$

It is immediately noted that for $k_1p_{CO} \gg k_{-1}$, $2k_4p_{O_2}$, we get the experimentally determined limiting form: Rate $= k_{-1}(T)$ $[(2k_4p_{O_2})/(k_1p_{CO})]$. This result was shown previously by Oh *et al.* (*26*) and McCabe and McCready (*59*). Herz and Marin (*39*) also showed an improved predicted rate dependence on CO if oxygen adsorption required one rather than two sites. Also, the apparent activation energy is given by

$$\varepsilon_a = -\frac{\beta E_\beta + 2\alpha\Gamma\varepsilon_{-1}}{\beta + 1 - 2\alpha\Gamma} = \varepsilon_{-1}\left(\frac{\beta - 2\alpha\Gamma}{\beta + 1 - 2\alpha\Gamma}\right). \quad (56)$$

Equation (56) reveals that the apparent activation energy is independent of the surface reaction constant, since $\alpha\Gamma = k_4p_{O_2}/k_{-1}$. This indicates that the key steps are molecular oxygen adsorption and CO desorption. For $k_1p_{CO} \gg k_4p_{O_2}$, Eq. (54) predicts that $\theta_{CO} \approx \beta/(1 + \beta)$; i.e., the CO coverage approaches its equilibrium value. In this limit the rate is controlled by molecular oxygen adsorption and the apparent activation energy (ε_a) is equal to the CO desorption activation energy (ε_{-1}).

As demonstrated below, at a high enough CO pressure the ER reaction steps can dominate the Langmuir reaction steps. The reason is straightforward: the elementary rates of ER steps (7) and (8) are proportional to the CO pressure and thus are unbounded in a sense. However, the rates of the Langmuir steps are bounded by the product of the coverages of the reactants. This point is expanded below. Despite this difference, it is easily shown that a mechanism consisting of steps (1), (4), (7), and (8) for the CO-covered surface gives a rate that is identical to Eq. (55) if $k_1p_{CO} \gg k_{-1}$, $2k_4p_{O_2}$.

The results of this analysis are at least kinetic evidence that molecular oxygen single-site adsorption competes with dissociative two-site adsorption in the CO inhibition regime. For the single-site process only one CO molecule must desorb to free-up a site for oxygen to adsorb. This gives a rate which is (-1) order in CO and first order in oxygen, and which has an activation energy equal to the CO binding energy.

A more detailed analysis of the predicted reaction order with respect to CO is now conducted. Experimental studies reveal a shift from an order of (-1) for the CO-covered surface to between 1 (*60, 3*) and as high as 4 (*7*) for the oxygen-covered surface. Figure 6 shows the predicted dependence of the CO order as a function of the CO pressure (β). The parameter values used are $\alpha = 10^{-4}$, $\gamma = 10^{-5}$, $\delta = 10^2$, and $\eta = 10^{-1}$. The value for γ approximates low pressure operation. The ER steps are assumed not to occur ($\xi = \kappa = 0$). Two values of Γ are considered, 10^{-10} and 5×10^{-6} $(= \gamma/2)$. The former value assumes that oxygen adsorption is dominated by the two-site dissociative step (i.e., model I); the latter value assumes equal sticking probabilities for molecular and atomic oxygen.

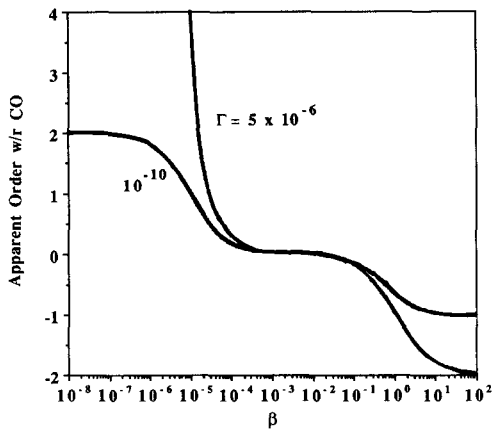

FIG. 6. Dependence of the apparent reaction order on β ($= k_1 p_{CO}/k_{-1}$) for case of negligible molecular oxygen adsorption ($\Gamma = 10^{-10}$) and case in which the sticking probability of molecular oxygen adsorption is equal to that of dissociative adsorption of oxygen ($\Gamma = \gamma/2 = 5 \times 10^{-6}$). Other parameter values provided in text.

For the first case ($\Gamma = 10^{-10}$) the predicted order shifts from -2 for large β to 2 for small β. This is a typical result for model I ($\Gamma = 0$). For a higher molecular oxygen sticking probability the order approaches (-1) for large β, as it should. This again suggests that single-site oxygen adsorption is necessary to predict the (-1) order for the CO inhibition regime ($\beta \gg 1$). For low CO pressure (β), or equivalently low CO coverage, the apparent reaction order gets very large for the $\Gamma = 5 \times 10^{-6}$ case. This means that the predicted rate approaches zero at a nonzero CO pressure (β). The reason for this behavior is as follows. Inspection of Eq. (39) for $\theta_{CO} \to 0$ reveals that the molecular oxygen coverage approaches the value Γ/δ ($= 5 \times 10^{-8}$). Thus, molecular oxygen occupies a small (but nonzero) fraction of the sites, but reacts at a negligible rate with CO due to the second-order reaction step (6) rate dependence on θ_{CO}. This site blocking by the molecular oxygen results in the highly nonlinear dependence of the rate on the CO pressure. Note that the assumed irreversibility of step (4) plays a pivotal role in this blocking. This point is considered in the model V analysis. These findings suggest that some other mechanism must exist to predict the observed near unity reaction order with respect to CO.

Some calculations are now presented which demonstrate that inclusion of the Eley–Rideal type reaction steps between gaseous or weakly adsorbed CO and adsorbed oxygen species is one modification that can predict the first-order rate dependence on CO pressure for a low CO/O_2 pressure ratio. The ER reaction between gas phase (or weakly adsorbed) CO and adsorbed oxygen (atomic and molecular) enables CO_2 to be much more easily produced from a surface that is primarily covered with oxygen. It can be shown analytically that when the ER reactions dominate for the oxygen covered surface the rate is zero order in oxygen, in agreement with experimental observations. Figure 7 shows the predicted dependence of the apparent CO reaction order on the dimensionless CO pressure. The dimensionless oxygen dissociative adsorption flux (Γ) is fixed at 5×10^{-6} ($= \gamma/2$). The other parameter values are the same as those in Fig. 6. The dimensionless ER rate constants, ξ and κ, are assigned values between 10^{-8} and 10^{-4}. Each case approaches the asymptotic orders of 1 and -1 for $\beta \to$

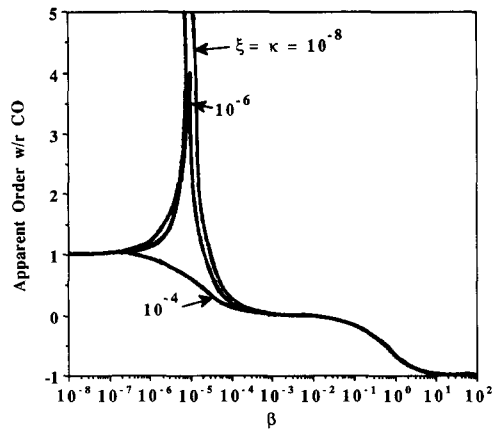

FIG. 7. Impact of Eley–Rideal rate constants ξ ($= k_7/k_1$) and κ ($= k_8/k_1$) on the dependence of apparent reaction order on β.

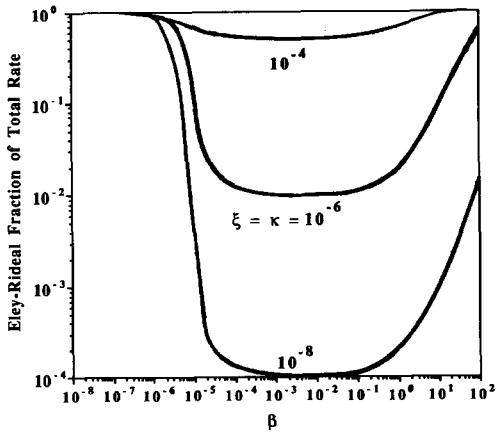

FIG. 8. Fraction of total rate attributed to Eley–Rideal reaction steps (7) and (8) for the three cases shown in Fig. 7.

0 and $\beta \gg 1$, respectively. For rather slow ER reactions ($\xi = \kappa \leq 10^{-6}$) the order exhibits a local maximum exceeding unity at an intermediate CO pressure. For rapid ER reactions, say $\xi = \kappa = 10^{-4}$, the order is bounded between 1 (for $\beta \to 0$) and -1 (for $\beta \gg 1$) and is a monotonic function of β. Note that inclusion of the ER steps corrects the unacceptable high reaction order with respect to CO predicted by a model consisting only of steps (1)–(6).

It is instructive to compute the fractional contribution to the total rate by the Eley–Rideal steps. The dimensionless total rate (r_D) is obtained by dividing the rate in Eq. (49) by k_3:

$$r_D = (\theta_{CO}\theta_O + 2\eta\theta_{CO}^2) + \left(\frac{\beta\xi}{\alpha}\theta_O + \frac{\beta\kappa}{\alpha}\theta_{O_2}\right). \quad (57)$$

Figure 8 shows the fractional contribution of the ER steps (7) and (8) to the overall rate for the three cases in Fig. 7. As expected, it is seen that the ER reaction path is quite competitive with the Langmuir path in the oxygen-covered surface regime. For intermediate CO pressures the Langmuir steps dominate. This Langmuir region expands as the ER reaction constants decrease. The same is true in the CO inhibition regime, except for very high CO/O_2. A comparison of the rates of Langmuir steps (3) and (6), and ER steps (7) and (8) helps to interpret these findings. If $\beta\xi/\alpha$ ($= k_7 p_{CO}/k_3$) $\gg \theta_{CO}$ and/or $\beta\kappa/\alpha$ ($= k_8 p_{CO}/k_3$) $\gg \theta_{CO}^2$, then the ER steps dominate. These conditions are satisfied if (i) the CO pressure is very large such that $\beta \gg \alpha/\xi$ ($p_{CO} \gg k_3/k_7$) and $\beta \gg \alpha/\kappa$ ($p_{CO} \gg k_3/k_8$), or (ii) the CO coverage is very small. In case (i) an upper bound of unity for the CO coverage enables the ER reaction to dominate at high CO pressures. In case (ii) the ER steps dominate as the CO pressure gets small relative to that for oxygen since the oxygen blocks CO adsorption.

MODEL III: MOLECULARLY ADSORBED OXYGEN WITH OXYGEN SITE EXCLUSION

A second means of predicting a reaction order of unity with respect to CO for a low CO/O_2 pressure ratio is to assume that the oxygen is excluded from a fraction of the sites. Studies reveal that the maximum coverage by adsorbed oxygen is 0.5 (e.g., (*61*, *62*)). Herz and Marin (*39*) proposed that oxygen excludes itself from a fraction of sites on supported metal catalysts.

Model Development

Model III adopts this oxygen site exclusion feature and retains model II steps (4)–(6) involving molecularly adsorbed oxygen. Equations (37)–(39) describe the steady-state balances for adsorbed CO, atomic, and molecular oxygen. The Eley–Rideal reaction steps (7) and (8) are neglected ($\xi = \kappa = 0$). The oxygen self-exclusion is accounted for by the parameters e and f in Eq. (40b). Adsorbed atomic and molecular oxygen are assumed to exclude a fraction $1/f$ of the sites for oxygen adsorption. This means that the maximum fraction of surface that can be occupied by oxygen species is $1/f$. The term e, given by

$$e = \frac{1 - f(\theta_O + \theta_{O_2})}{1 - (\theta_O + \theta_{O_2})} \quad (58)$$

accounts for CO adsorbed on empty sites that an adjacent oxygen (atomic or molecular) excludes for oxygen adsorption. The CO does not block such a site for oxygen adsorption. Based on UHV evidence, it is assumed that CO can occupy all the sites. Equation (50) is an approximate single function representation of model III (i.e., $e = 1$ is a good approximation in many cases). Otherwise, the three original Eqs. (37)–(40) must be solved simultaneously.

It should be pointed out that Gorte and Schmidt (*63*) proposed a modification of oxygen adsorption–desorption involving a precursor. Kaul *et al.* (*36*) adopted this feature in their model. This limits the saturation coverage similar to the oxygen exclusion feature of model III. However, this feature does not correct the behavior in the CO inhibition regime.

Kinetic Analysis

Model III predicts the correct limiting reaction orders with respect to CO (see (*51*)). The main points are demonstrated by examining limiting behaviors.

Suppose we consider the sequence involving only adsorbed molecular oxygen (steps (1), (4), and (6)), which is a good approximation for the CO-covered surface. The maximum coverage of oxygen is $1/f$. The dimensionless CO and oxygen balances are given by

$$\beta(1 - \theta_{CO} - \theta_{O_2}) - \theta_{CO} - 2\eta\alpha\theta_{CO}^2\theta_{O_2} = 0 \quad (59)$$

$$\Gamma(1 - e\theta_{CO} - f\theta_{O_2}) - \eta\theta_{CO}^2\theta_{O_2} = 0, \quad (60)$$

where e is given by Eq. (58) with $\theta_O = 0$. Following earlier developments, for sufficiently low temperature the CO coverage approaches its adsorption–desorption equilibrium value. This value is given by Eq. (59) assuming the reaction term is sufficiently smaller than the adsorption or desorption terms; i.e., $\theta_{CO} = \beta(1 - \theta_{O_2})/(1 + \beta)$. Substituting this into Eq. (60) gives

$$\theta_{O_2}[\eta\beta^2(1 - \theta_{O_2})^2 + f\Gamma(1 + \beta)^2] - \Gamma(1 + \beta)(1 + f\beta\theta_{O_2}) = 0. \quad (61)$$

If we assume further that the coverage of oxygen is small ($\theta_{O_2} \ll 1$) then Eq. (61) gives

$$\theta_{O_2} = \frac{\Gamma(\beta + 1)}{\eta\beta^2 + f\Gamma(\beta + 1)}. \quad (62)$$

The reaction rate is then

$$\text{Rate} = \frac{2k_6(T)\Gamma/\eta[\beta^2 + (f - 1)\Gamma(1 + \beta)/\eta]^2}{(1 + \beta)[\beta^2 + f\Gamma(1 + \beta)/\eta]^3}. \quad (63)$$

Equation (63) predicts that if $k_6k_1p_{CO}/k_{-1} \gg fk_4p_{O_2}$, then the rate has the same pressure and temperature dependence observed experimentally: it is proportional to p_{O_2}/p_{CO} with an apparent activation energy equal to the CO binding energy (E_{-1}). However, if $\beta \gg 1$ but $fk_4p_{O_2}$ is on the same order as $k_6k_1p_{CO}/k_{-1}$, then the rate is given by

$$\text{Rate} = \frac{2k_4p_{O_2}[\beta + \Gamma(f - 1)/\eta]^2}{[\beta + f\Gamma/\eta]^3}. \quad (64)$$

Equation (64) reveals a less obvious dependence if the oxygen pressure is sufficiently large, or the surface reaction constant is small compared to the oxygen adsorption flux.

For $f > 1$ model III predicts a first-order dependence on CO pressure for $p_{CO}/p_{O_2} \ll 1$. The reason is straightforward: A fraction of sites equal to $(1 - 1/f)$ is made available for CO adsorption that is inaccessible to the oxygen; the rate is given by the form $kp_{CO}(1/f)$.

Model IV: CO and Oxygen Site Exclusion

This model incorporates the oxygen site exclusion feature of model III with CO site exclusion into the basic three-step model (I). Graham and Lynch (*32*) demonstrated that a CO site exclusion model did the best job of fitting multiple steady-state data for CO oxidation on Pt/Al_2O_3 in a stirred reactor. In this section we demonstrate the detailed kinetic features in the two limiting regimes of low and high CO/O_2 pressure ratio. It should be noted that although there is evidence for incomplete oxygen coverage

on both supported and unsupported catalysts, evidence for CO site exclusion has been found only for supported catalysts (*64, 65*).

Model Development

The CO and atomic oxygen balances are respectively described by

$$\beta(1 - \theta_{CO} - \theta_O)\frac{(1 - n\theta_{CO})}{(1 - \theta_{CO})} - \theta_{CO} - \alpha\theta_{CO}\theta_O = 0 \quad (65)$$

$$\gamma\frac{(1 - f\theta_O)^2}{(1 - \theta_O)^2}(1 - \theta_{CO} - \theta_O)^2 - \theta_{CO}\theta_O = 0. \quad (66)$$

The new CO adsorption term in (65) accounts for exclusion of sites for CO adsorption by CO itself. The term also accounts for the oxygen adatoms that do not block CO adsorption *per se* since they are on sites that adjacent CO adsorbates exclude for CO adsorption.

Kinetic Analysis

For the oxygen-covered surface ($\theta_{CO} \to 0$) Eqs. (65) and (66) are combined to give

$$\alpha\gamma f^2\theta_O^2 + (\beta - 2f\alpha\gamma)\theta_O + \alpha\gamma - \beta = 0. \quad (67)$$

The rate is given by

$$\text{Rate} = k_3\frac{\beta}{\alpha}(1 - \theta_O) = k_1 p_{CO}(1 - \theta_O). \quad (68)$$

The maximum coverage of atomic oxygen is $1/f$. Clearly, Eq. (68) predicts that the rate is first order in CO and zero order in oxygen. The agrees with experimental observations (*3*).

For the CO-covered surface the oxygen coverage is small and the CO coverage approaches its equilibrium value of $\beta/(1 + n\beta)$. Applying this to Eq. (66) gives the quadratic expression in θ_O:

$$[\gamma f^2(1 + n\beta)^2]\theta_O^2 - [2f\gamma(1 + n\beta)(1 + (n - 1)\beta) + \beta(1 + n\beta)]\theta_O + \gamma[1 + (n - 1)\beta]^2 = 0. \quad (69)$$

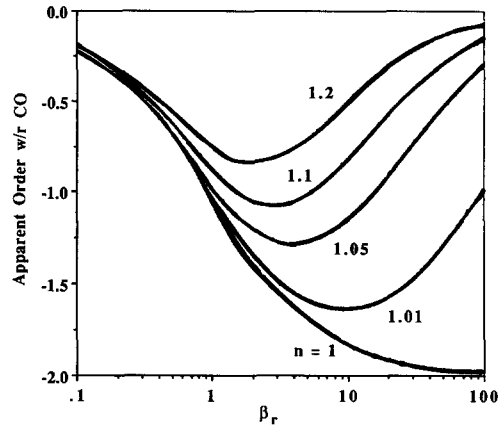

FIG. 9. Model IV predictions of the dependence of the apparent CO reaction order on dimensionless CO pressure (β) for five values of the CO self-exclusion parameter (n).

If $\theta_O \to 0$, the first term in (69) can be neglected. Solution for θ_O gives

$$\theta_O = \frac{\gamma[1 + (n - 1)\beta]^2}{2f\gamma(1 + n\beta)(1 + (n - 1)\beta) + \beta(1 + n\beta)}. \quad (70)$$

The rate is then

$$\text{Rate} = 2k_2 p_{O_2}\left(\frac{\beta}{1 + n\beta}\right)\left\{\frac{[1 + (n - 1)\beta]^2}{2f\gamma(1 + n\beta)(1 + (n - 1)\beta) + \beta(1 + n\beta)}\right\}. \quad (71)$$

Equation (71) predicts that the CO order is bounded between -2 and 0. If $n = 1$ and $f = 1$ (no CO or oxygen exclusion) we recover the earlier result for model I that the rate is (-2) order in CO. This result is true for any reasonable f value ($f < 5$) by inspecting Eq. (71). For $n > 1$ there is CO exclusion. This permits oxygen to adsorb more easily because of a freeing-up of empty sites inaccessible for CO adsorption. This increases the order with respect to CO to a value as high as zero.

Figure 9 shows the calculated dependence of the CO reaction order on the dimensionless CO pressure (β) for several values

of the CO exclusion parameter (n). For these calculations we solved Eqs. (65) and (66) for θ_{CO} and θ_O simultaneously. The other parameter values are $f = 2$, $\alpha = 10^{-4}$, and $\gamma = 10^{-5}$. Only β values exceeding 0.1 are shown to focus on the CO inhibition regime. All the curves approach one another for $\beta < 0.1$. For $\beta \to 0$ the order approaches unity, as discussed above. Figure 9 confirms the analytic result (Eq. (71)) that the CO order for $\beta \gg 1$ is bounded between 0 ($n > 1$) and -2 ($n = 1$). For $n > 1$ the order exhibits a local minimum at an intermediate β value. For $\beta \to \infty$ the order approaches zero. Under these conditions the rate is controlled by the adsorption of oxygen to surface sites that are inaccessible for CO adsorption.

Model V: Equilibrated Molecular Oxygen Adsorption

In model II it was assumed that oxygen adsorbs irreversibly both by a direct dissociative route and by a two-step molecular precursor mechanism. Also, reaction of adsorbed molecular oxygen and CO is termolecular. In this final model V these features are reexamined.

Model Development

The model V sequence consists of reversible CO adsorption (step (1) in (1)), reversible molecular adsorption (step (4) in (36)), irreversible oxygen dissociation (step (5) in (36)), ER-type reactions (steps (7) and (8) in (36)), reaction step (3) (in (1)), and the bimolecular reaction step

$$(9): \text{CO}\text{–}X + \text{O}_2\text{–}X \to \text{CO}_2 + \text{O}\text{–}X + X. \tag{72}$$

The two new features of model V are (i) oxygen adsorbs by the single route in which it first equilibrates as a molecular species and can then irreversibly dissociate, and (ii) the reaction between adsorbed CO and molecular oxygen is bimolecular.

Regarding feature (i), dissociative adsorption by way of an adsorbed molecular species is the well-known Lennard-Jones mechanism (*66*). Ceyer (*67*) recently discussed the mechanism and its implications during the steam reforming of methane on nickel. Equilibration of the molecular oxygen adsorption step is expected if the rates of adsorption and desorption significantly exceed its consumption by dissociation or by reaction. A key point is that adsorption equilibrium ensures a second-order vacant site dependence for the rate of the dissociation step. Without it, the model does not necessarily admit multiple solutions if the direct dissociation step (2) (from models I–IV) is not included in the sequence. Regarding feature (ii), a bimolecular reaction between adsorbed CO and molecular oxygen is probably more plausible than the termolecular reaction step of models II and III.

The adsorbed CO, and adsorbed atomic and molecular oxygen balances are given by

$$\beta\theta_v - \theta_{CO} - \alpha\theta_{CO}\theta_O - \alpha\tau\theta_{CO}\theta_{O_2} = 0 \tag{73}$$

$$2\delta\theta_{O_2}\theta_v - \theta_{CO}\theta_O + \tau\theta_{CO}\theta_{O_2} - \frac{\xi\beta}{\alpha}\theta_O + \frac{\kappa\beta}{\alpha}\theta_{O_2} = 0 \tag{74}$$

$$\Gamma\theta_v - \delta\theta_{O_2}\theta_v - \tau\theta_{CO}\theta_{O_2} - \psi\theta_{O_2} - \frac{\kappa\beta}{\alpha}\theta_{O_2} = 0, \tag{75}$$

where two new parameters (τ and ψ) are defined as

$$\tau = \frac{k_9}{k_3} \quad \psi = \frac{k_{-4}}{k_3}. \tag{76}$$

If rapid equilibration of step (4) is assumed, then Eq. (75) simplifies to

$$\theta_{O_2} = \frac{\Lambda}{1 + \Lambda}(1 - \theta_{CO} - \theta_O), \tag{77}$$

where Λ is a dimensionless molecular oxygen adsorption equilibrium constant,

$$\Lambda = \frac{\Gamma}{\psi} = \frac{k_4 p_{O_2}}{k_{-4}}. \tag{78}$$

Substitution of (77) into (73), followed by solution for θ_O, gives

$$\theta_O = \frac{(1 + \Lambda)\theta_{CO} + \alpha\tau\Lambda\theta_{CO}(1 - \theta_{CO}) - \beta(1 - \theta_{CO})}{\alpha\tau\Lambda\theta_{CO} - \alpha(1 + \Lambda)\theta_{CO} - \beta}. \quad (79)$$

Substitution of (79) into (74) gives the single-state variable function

$$F(\theta_{CO}, \theta_O(\theta_{CO}), \mathbf{p}) = \frac{2\delta\Lambda}{(1 + \Lambda)^2}(1 - \theta_{CO} - \theta_O)^2 - \theta_{CO}\theta_O + \frac{\tau\Lambda}{(1 + \Lambda)}\theta_{CO}(1 - \theta_{CO} - \theta_O) - \frac{\xi\beta}{\alpha}\theta_O + \frac{\kappa\beta\Lambda}{\alpha(1 + \Lambda)}(1 - \theta_{CO} - \theta_O) = 0. \quad (80)$$

For a given $\mathbf{p}$, Eq. (80) must be solved for θ_{CO}. The dimensionless rate (r_D) is given by

$$r_D = \theta_{CO}\theta_O + \tau\theta_{CO}\theta_{O_2} + \frac{\xi\beta}{\alpha}\theta_O + \frac{\kappa\beta}{\alpha}\theta_{O_2}. \quad (81)$$

Kinetic Analysis

In the limit of an oxygen-covered surface the molecular oxygen coverage approaches zero (Eq. (77)). Thus, the rate is bounded between 1 and 2 depending on the rate of the ER step (7) relative to the Langmuir step (3). The proportionality between molecular oxygen and vacant site coverage also eliminates the undesirable molecular oxygen site blocking feature when step (4) is irreversible and the ER steps are slow, which is the case for models II and III.

In the limit of a CO-covered surface the analysis is more involved. If we neglect the ER steps and further assume CO approaches adsorption equilibrium, then θ_{CO} satisfies

$$\theta_{CO} = \frac{\beta}{1 + \Lambda + \beta}. \quad (82)$$

The latter assumption is likely to be valid for $\beta \gg \Lambda + 1$. Use of Eq. (82) in (77), and assuming that $\theta_O \ll \theta_{CO}, \theta_{O_2}$, gives the result

$$\theta_{O_2} = \frac{\Lambda}{1 + \Lambda + \beta}. \quad (83)$$

Use of Eq. (82) and (83) in Eq. (74) gives

$$\theta_{CO}\theta_O = \frac{2\delta\Lambda + \tau\Lambda\beta}{(1 + \Lambda + \beta)^2}. \quad (84)$$

The rate is then given by

$$\text{Rate} = k_3\theta_{CO}\theta_O + k_9\theta_{CO}\theta_{O_2} = \frac{2\Lambda}{(1 + \Lambda + \beta)^2}[k_5 + k_9\beta]. \quad (85)$$

Rate equation (85) has two limiting forms. First, if $k_5 \gg k_9\beta$, then

$$\text{Rate} = k_5\frac{2\Lambda}{(1 + \Lambda + \beta)^2}. \quad (86)$$

Further, if $\beta \gg 1 + \Lambda$, Eq. (86) predicts that rate $\propto (p_{CO})^{-2}p_{O_2}$, with an apparent activation energy equal to $E_5 + 2E_{-1} + E_{-4}$. The second more likely case is if $k_5 \ll k_9\beta$, for which the rate is

$$\text{Rate} = k_9\frac{2\Lambda\beta}{(1 + \Lambda + \beta)^2}. \quad (87)$$

If $\beta \gg 1 + \Lambda$, Eq. (87) predicts that rate $\propto (p_{CO})^{-1}p_{O_2}$, in agreement with experimental observation. The predicted apparent activation energy is equal to $E_{-1} + E_9 - E_{-4}$. This does not agree with the experimental value of E_{-1}, unless $E_9 - E_{-4}$ fortuitously vanishes. If E_{-4} is less than 10 kcal/mol, given that adsorbed molecular oxygen is weakly bound and E_9 is on the order of 15–25 kcal/mol then the apparent activation energy would not be far from the experimental value, but would still be too high. Finally, an analysis of the CO-covered surface regime when the ER reactions dominate reveals for a sufficiently high CO pressure that rate $\propto p_{O_2}$; i.e., the rate is zero order with respect to CO. Thus, unlike model II, model V predicts that the qualitative kinetic behavior in the CO-covered surface regime is altered if the ER reactions dominate the Langmuir reactions. This may suggest that molecular oxygen adsorption equilibrium is not established in this regime.

Sample simulations of the CO reaction order as a function of the CO pressure (β)

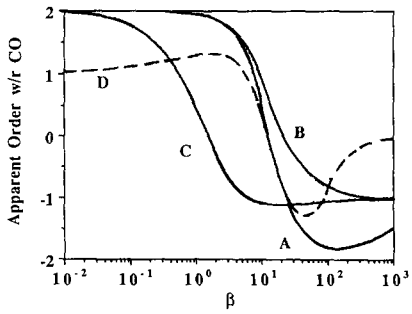

FIG. 10. Model V predictions of the dependence of the apparent CO reaction order on the dimensionless CO pressure (β) for four cases labeled A–D. For all cases $\Lambda = 1$ and $\alpha = 10^{-4}$. The values of τ and δ assume the values of 0.1 and 100 for cases A and D, 10 and 100 for case B, and 0.1 and 1 for case C. The ER parameters ξ and κ are zero except for case D, for which $\xi = \kappa = 10^{-6}$.

are shown in Fig. 10. The parameters τ ($= k_9/k_3$), ξ ($= k_7/k_1$), and κ ($= k_8/k_1$) are varied to illustrate several of the trends discussed above; their values are noted in the Fig. 10 caption. The remaining parameters Λ ($= k_4 p_{O_2}/k_{-4}$) and α ($= k_3/k_{-1}$) are fixed at 1 and 10^{-4}, respectively. The small values for α ensures a single-valued rate (refer to discussion of Fig. 2).

At low CO pressure (β) the order approaches 2 if the ER reactions do not occur (cases A, B, and C in Fig. 10), and unity if the ER reactions are competitive with the Langmuir reactions (case D). At high CO pressure the limiting order approaches -1 if reactions occurs primarily between adsorbed CO and molecular oxygen; i.e., reaction can proceed without requiring oxygen to dissociate first. This occurs if $\tau\beta \gg \delta$, a condition which results in limiting rate expression (87), and which is satisfied by cases B ($\tau = 10, \delta = 100$) and C ($\tau = 0.1, \delta = 1$) for $\beta > 100$. On the other hand, if $\tau\beta \ll \delta$ then rate equation (86) is satisfied, which predicts a CO order that approaches -2 in the CO-covered surface regime. This is true for case A ($\tau = 0.1, \delta = 100$) for $\beta \approx 10^2$. Finally, case D shows that if the ER reactions dominate the CO order approaches zero for sufficiently large β.

COMPARISON OF THE MODELS

A comparison of the rates predicted by models I–IV provides some insight about the importance of various steps in the four sequences. (Model V is not considered here). Figure 11 compares and contrasts the features of a model I case ($\Gamma = 10^{-10}$ in Fig. 6), a model II case ($\xi = \kappa = 10^{-4}$ in Fig. 7), a model III case ($f = 2$), and a model IV case ($n = 1.1$ in Fig. 9). The dependence of the rate (Eq. (57)) on the CO pressure (β) is shown. The parameters common to the models assume the values $\alpha = 10^{-4}$, $\gamma = 10^{-5}$, and $\phi = 0$. For models II and III, $\delta = 10^2$ and $\eta = 10^{-1}$.

The predicted rate exhibits a maximum over a large intermediate range of CO pressure for each case. The rate declines in the two extremes of low and high CO pressure (β). The model II and III rates exceed the model I rate for the entire β range. The model II and III rates are virtually identical for sufficiently large β ($>10^{-3}$). This indicates that for this β range the same process is rate-controlling (oxygen adsorption and/or CO desorption) despite the additional ER path for model II. The model III and IV rates are nearly identical for $\beta < 10^{-5}$. This demonstrates that for low β the key process

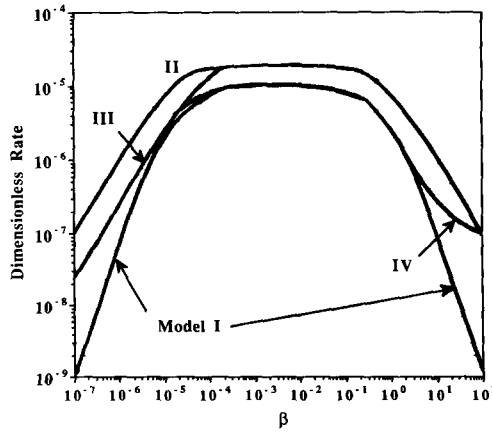

FIG. 11. Comparison of the dimensionless rate dependence on β for the $\Gamma = 10^{-10}$ case in Fig. 6, a model II case ($\xi = \kappa = 10^{-4}$ in Fig. 7), a model III case ($f = 2$), and a model IV case ($n = 1.1$ in Fig. 9).

is oxygen site exclusion. Models I and IV exhibit virtually the same rates over a large intermediate β range (10^{-3} – 1), showing that exclusion is not important for this CO pressure range.

Models I–IV predict that the rate is close to zero order in CO for an intermediate range of CO pressure. The model I case reveals the second-order dependence on CO for low β and the (−2) order for high β. Models II and III predict a first-order dependence for low β and a (−1) order for high β. These typical results demonstrate the capability of models II and III of predicting the correct asymptotic CO orders. Model IV predicts a first-order dependence on CO for low β but an order that exhibits a local minimum for $\beta \approx 3$ and that approaches zero for $\beta \geq 100$. A key point to note is that each model predicts that for low β, $\theta_{O_2} \rightarrow \Gamma/\delta$ ($= 5 \times 10^{-8}$). In the high CO pressure regime ($\beta > 1$), θ_{O_2} gradually decreases and approaches the coverage of atomic oxygen. This shows that a small fraction of vacant sites makes single-site molecular oxygen adsorption (step (4)) competitive with two-site dissociative oxygen adsorption for the CO-covered surface.

MULTIPLICITY ANALYSES OF MODELS II–V

Developments above indicate that the modifications of the basic three-step model I in models II–V remedy the three-step model I flaws in not being able to predict the basic experimental kinetic features. A key question is what impact these modifications have on the predicted rate multiplicity features. The new models should be able to predict the experimental multiplicity features when the parameters associated with the new steps are assigned values that enable the correct prediction of the basic kinetic features. The following analyses underscore the requirement of two vacant sites for oxygen adsorption and of a Langmuir reaction step if intrinsic rate multiplicity is to be predicted.

Model II. A kinetic model which consists of steps (1), (4), and (6) is one in which oxygen is only adsorbed molecularly and the surface reaction is termolecular. Equations (37)–(39) reduce to this case by setting θ_O, γ, δ, ξ, and κ equal to zero. It is easily shown that the solution of this limiting case is a quadratic function of the CO coverage. The function has a unique feasible root for a given set of feasible parameters. A kinetic model which consists of steps (1), (2), and (7) is one in which oxygen dissociatively adsorbs but the reaction is assumed to proceed by the ER mechanism only. It is easily shown that the solution is also a quadratic function of the CO coverage. The function has a unique feasible root for a given set of feasible parameters, and multiplicity cannot be predicted. Moreover, in the regime of negligible oxygen coverage the rate has a negative second-order dependence on CO, and the apparent activation energy is twice the CO desorption activation energy.

TABLE 3

Base Set of Parameter Values Used in Analysis of Multiplicity Features of Eight-Step Model

$\alpha_r = 10^4$	$E_\alpha = -15$
$\gamma_r = 10^{-4}$	$E_\gamma = -15$
	$E_\beta = -30$
$\delta = 10^2$	$\eta = 1$
$\Gamma_r = 5 \times 10^{-5}$	$\xi = \kappa = 0$

These points are illustrated by examining the impact of the molecular oxygen and the Eley–Rideal reaction steps on the multiplicity features. Table 3 lists the base set of parameter values used.

Figure 12 shows the influence of the molecular oxygen sticking probability (Γ_r) on the temperature (y)–CO pressure (β_r) bifurcation map. If $\Gamma_r = 0$ the model reverts to the basic version. For $\Gamma_r = 5 \times 10^{-5}$ ($= \gamma_r/2$) the sticking probability of molecular oxygen adsorption is assumed equal to that for dissociative oxygen adsorption. As Γ_r increases, the multiplicity region shrinks and moves to higher CO pressures. For suf-

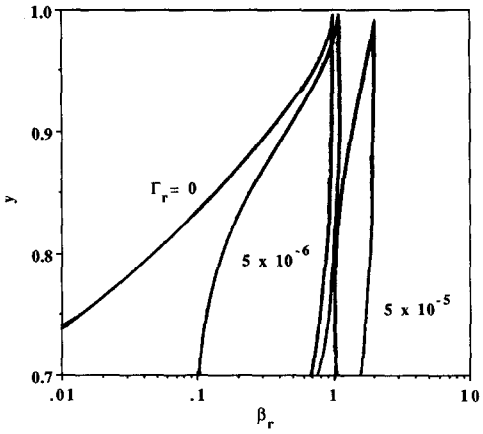

FIG. 12. Impact of the molecular oxygen sticking probability (Γ_r) on the temperature (y)–CO pressure (β_r) bifurcation map. Other parameter values shown in Table 3.

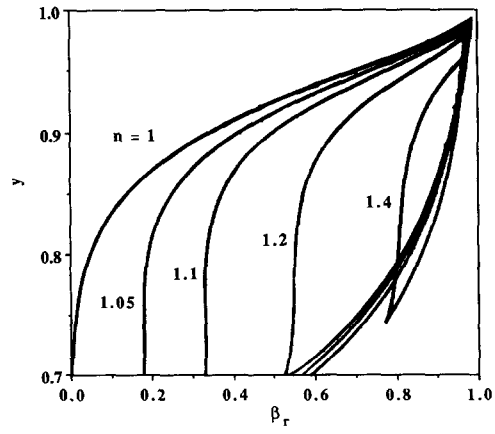

FIG. 14. Impact of the CO self-exclusion parameter (n) on the y–β_r bifurcation map. Other parameter values are shown in Table 3.

ficiently large values of Γ_r (up to 10^{-2}) the multiplicity region becomes vanishingly thin, confirming the analytical predictions.

The impact of the Eley–Rideal reaction steps (7) and (8) is shown in Fig. 13. The corresponding dimensionless rate constants ξ ($= k_7/k_1$) and κ ($= k_8/k_1$) are set equal and increased from 0 to 100. The region moves to lower CO pressures and shrinks in size. The $\xi = \kappa = 100$ case map has a high and low temperature cusp. For a sufficiently large $\xi = \kappa$ it can be shown that multiplicity does not exist for any CO pressure. This is supported by a predicted lack of multiplicity for the model comprised of steps (1), (2), and (7).

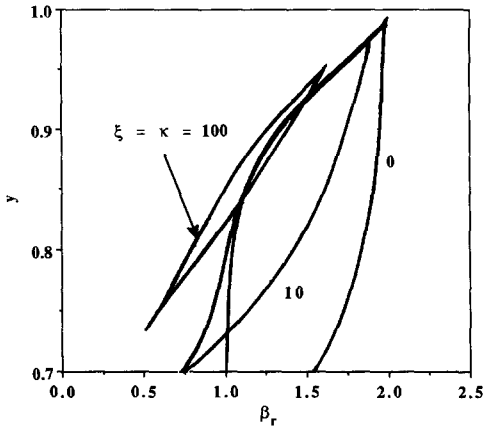

FIG. 13. Impact of the Eley–Rideal reaction step rate constants (ξ and κ) on the y–β_r bifurcation map. Other parameter values are shown in Table 3.

Model III. The impact of the extent of oxygen site exclusion (magnitude of parameter f) on the multiplicity features qualitatively resembles Fig. 13 (*51*). The region of multiplicity in the $y - \beta_r$ plane shrinks as f increases from unity to 100. As the surface becomes increasingly incapable of admitting oxygen ($\theta_O + \theta_{O_2} \leq 1/f \rightarrow 0$) the region of multiplicity vanishes. This demonstrates that the key nonlinearity is the two-site requirement for dissociative oxygen adsorption.

Model IV. The impact of CO exclusion on the $y - \beta_r$ bifurcation map is shown in Fig. 14 for a typical case. These maps were constructed by solving for the singular set defined by Eq. (15), where the steady-state function F is determined by combining Eqs. (65) and (66),

$$F(\theta_{CO}, \theta_O, \mathbf{p}) = \gamma(1 - \theta_{CO} - \theta_O)^2(1 - f\theta_{CO})^2 - \theta_{CO}\theta_O(1 - \theta_O)^2 = 0, \quad (88)$$

where

$$\theta_O = \frac{\beta(1 - \theta_{CO})(1 - n\theta_{CO}) - \theta_{CO}(1 - \theta_{CO})}{\beta(1 - n\theta_{CO}) + \alpha\theta_{CO}(1 - \theta_{CO})}. \quad (89)$$

All parameters are assigned the values in Table 3 except that oxygen does not adsorb molecularly ($\Gamma_r = 0$). Also, oxygen excludes itself from half the surface ($f = 2$). As n is increased the size of the multiplicity region decreases. The $n = 1.4$ map has two cusp points forming a region that resembles the $\xi = \kappa = 100$ case in Fig. 13. For a sufficiently large n our calculations reveal that multiplicity vanishes. These trends suggest that as the surface becomes increasingly inaccessible for CO, the range of CO pressure giving a low rate state decreases. This makes multiplicity less likely.

Model V. The earlier model development shows that with the molecular oxygen coverage equal to its equilibrium value (Eq. (77)) the oxygen adsorption step is second order in the vacant site coverage (Eq. (80)). The resulting single-state variable function is a fourth-order polynomial in θ_{CO}, and admits multiple feasible solutions. It can be shown that model V predicts the correct isothermal multiplicity features, such as the inverted cusp T–p_{CO} bifurcation map. Figure 15 shows sample multivalued dimensionless rate–CO pressure (β) bifurcation diagrams obtained by solving Eqs. (80) for θ_{CO} and using Eqs. (77), (79), and (81). The dimensionless oxygen adsorption equilibrium constant (Λ) is varied as a parameter. The other parameters assume the values $\alpha = 10^2$, $\tau = 10^{-1}$, $\delta = 10^2$, and $\xi = \kappa = 10^{-6}$. The diagrams have the expected clockwise hysteresis pattern. With increasing oxygen pressure (Λ) the range of β giving three solutions expands and moves to higher values. Note that the oxygen-covered surface (low β) the order with respect to CO (oxygen) is approximately 2 (− 1). This indicates that the Langmuir reactions dominate the ER reactions since such kinetic behavior is predicted by the three-step model I.

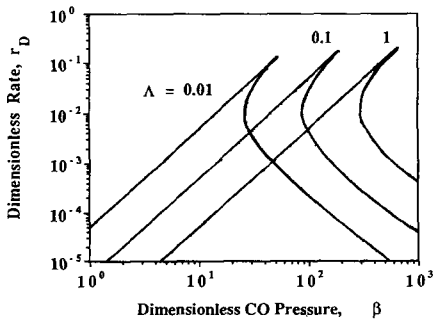

FIG. 15. Example of the model V predicted multivalued dependence of the dimensionless rate (r_D) on CO pressure (β) for several values of Λ. The other parameters assume the values $\alpha = 10^2$, $\delta = 10^2$, $\tau = 0.1$, and $\xi = \kappa = 10^{-6}$.

CONCLUDING REMARKS

This study demonstrates the importance of satisfying the basic kinetic features in the development of potential mechanistic sequences to model Pt-catalyzed CO oxidation. Correct prediction of the experimental multiplicity features alone is an insufficient discrimination tool. We have demonstrated that the widely used three-step model (I), while capably predicting the qualitative multiplicity features, cannot predict several basic kinetic trends. Four new sequences built upon the model I framework have been developed that predict the observed kinetic and rate multiplicity features.

The failure of the three-step model I to predict the correct kinetic behavior in the CO inhibition regime has been remedied two different ways.

The first modification is to assume that CO excludes itself from some of the sites (model IV), a physical picture that is more tenuous.

The second more plausible modification incorporates adsorption, dissociation, and reaction steps involving molecular oxygen (models II, III, and V) into the basic three-step model. It is shown for models II and III that the molecular oxygen/atomic oxygen coverage ratio is typically only nonnegligible if the coverage of CO is nearly complete. This is logical since these are the conditions when single-site molecular adsorption is

most competitive with two-site dissociative adsorption. Model V may be more firmly rooted on physical chemistry grounds than models II and III since oxygen adsorbs by the single molecular precursor route, and reaction between adsorbed CO and molecular oxygen is bimolecular. However, the models II and III predicted kinetic behavior in the CO-covered surface regime is in better agreement with experiment. Moreover, with only a single oxygen adsorption route, the molecular oxygen adsorption step must be at equilibrium to guarantee a multiplicity of solutions. These facts suggest that molecular oxygen adsorption equilibrium is not attained when the surface is covered with CO. Indeed, a hybrid of models II and V in which molecular oxygen adsorption equilibrium is not assumed *a priori* may mediate these issues. In any case, this first major modification of the basic three-step sequence relies on indirect kinetic evidence. Unfortunately, direct spectroscopic evidence may not be possible since the molecular oxygen coverage is minute compared to the CO coverage. Another interesting finding is that the model II predicted behavior in the CO inhibition regime is unaltered if the ER-type reactions are the dominant reaction path. This also illustrates the experimental challenge of proving a mechanism.

The three-step model I also fails to predict a first-order rate dependence on CO pressure for a primarily oxygen covered surface. Incorporation of (i) an Eley–Rideal type reaction between gas phase CO and adsorbed oxygen species (models II and V), or (ii) oxygen site exclusion (models III and IV) remedies this flaw. The model II calculations reveal that the ER reaction steps are important if the surface is primarily covered with oxygen ($p_{CO}/p_{O_2} \to 0$) or for $p_{CO} \gg p_{O_2}$. The Langmuir steps dominate otherwise. Models III and IV predict that the inaccessibility of a fraction of the sites for oxygen adsorption enables CO to adsorb and react with a first-order rate dependence.

Admittedly, some of the steps in the new models may not be truly elementary (e.g., ER reactions), or their existence may be impossible to prove by spectroscopic means. Nevertheless, the kinetic evidence for their existence is strong. Moreover, to the best of our knowledge, there is no experimental evidence to definitively rule out the proposed models (except possibly for CO site exclusion). We should point out that an implicit assumption in all the models is that the catalytic site is the same in all the elementary steps. There may be some motivation for reexamining this assumption in light of the fact that oxygen and CO adsorb at different locations on Pt single crystals.

Singularity theory is shown to be quite useful in unravelling the complex multiplicity features of a nonlinear kinetic model. A new means of locating regions in parameter space where different shapes of temperature–CO pressure bifurcation maps are obtained is presented. Such a procedure is very useful in the rational development of kinetic models capable of predicting experimentally observed multiplicity features and in the estimation of kinetic parameters. The alternative is a trial and error search in parameter space for the proper "combination" that predicts the correct features.

In the second part of this two-part study (*1*) models II and III are compared in a detailed analysis of several sets of CO oxidation rate data obtained under UHV, intermediate, and atmospheric pressure conditions. This essential step helps to link the kinetics of Pt-catalyzed CO oxidation observed in surface science conditions to higher pressure operation.

APPENDIX A: LIST OF NOTATION

a	term defined in Appendix B
b	term defined in Appendix B
c	term defined in Appendix B
e	parameter defined in Eq. (58)
E_i	activation energy of step i
E_j ($j \equiv \alpha$, β, etc.)	dimensionless activation energy for parameter j ($j \equiv \alpha$, β, etc.)
ER	Eley–Rideal

f	oxygen site exclusion parameter
f_{ij} (i = 1, 2; j = 1, 2, 3)	terms defined in Eq. (49a)–(49f)
F	steady-state function (e.g., Eq. (13))
G_k (k = 1, 2)	functions defined in Eqs. (46) and (47)
k	lumped rate constant
k_i (i = 1, −1, 2, −2, 3–8)	rate constant of step i
K	adsorption equilibrium constant
L	Langmuir
M	molecular weight
n	CO site exclusion parameter
p	pressure
$\mathbf{p}$	vector of parameters
q_i (i = 1 − 8)	terms defined in Appendix B
Q	term defined for isola variety nondegeneracy condition
r	reaction rate
R	Universal gas constant
S	sticking probability
T	temperature
U	function defined in Appendix B
V	steady-state function defined in Eq. (50)
X	denotes site on catalyst surface
X_i ($i \equiv \alpha$, β, γ, ϕ, δ, η, Γ)	exponential functions of temperature for parameter i
y	dimensionless temperature

Greek

α	parameter defined in (11)
β	parameter defined in (11)
δ	parameter defined in (41)
Δ	discriminant defined in (32)
ε_i ($i \equiv -1$, −2, 3, 5, 6)	dimensionless activation energy for step i
ϕ	parameter defined in (11)
γ	parameter defined in (11)
Γ	parameter defined in (41)
η	parameter defined in (41)
κ	parameter defined in (44)
λ	bifurcation parameter
Λ	dimensionless molecular oxygen adsorption equilibrium constant
θ	surface coverage
τ	parameter defined in (76)
ξ	parameter defined in (44)
Ψ	parameter defined in (76)

Subscripts

a	apparent
b	bulk
c	cusp
CO	carbon monoxide
D	dimensionless
I	isola
l	lower bound
O	atomic oxygen
O_2	molecular oxygen
r	reference
sr	surface reaction
v	vacant

APPENDIX B

a. Singular Set for Three-Step Model I

The steady-state function (Eq. (9)) is derived by combining the nondimensional forms of Eqs. (3)–(5); Eq. (5) gives $\theta_v = 1 - \theta_{CO} - \theta_O$, which is substituted into (3) and (4). θ_O is solved for in terms of θ_{CO} in (3), giving Eq. (12). This result is substituted into Eq. (4). Algebraic manipulations gives the fourth-order polynomial (Eq. (13)).

Differentiation of Eq. (13) with respect to θ_{CO} gives

$$\frac{dF}{d\theta_{CO}} = 4\theta_{CO}^3[\alpha^2\gamma] + 3\theta_{CO}^2[\alpha(\beta + 1) - 2\gamma(\alpha + 1)] + 2\theta_{CO}[\gamma(\alpha + 1)^2 + \beta(\beta + 1 - \alpha) - \phi(\beta + 1)^2] - [\beta(\beta - 2\phi(\beta + 1))] = 0. \quad (B.1)$$

The singular set is given by the simultaneous solution of Eqs. (13) and (B.1). An explicit form is derived as follows. The param-

eter γ is solved for in (B.1). This result is substituted into Eq. (13), giving the following quadratic expression in β:

$$a\beta^2 + b\beta + c = 0 \qquad \text{(B.2)}$$

$$\begin{aligned} a = {} & [\tfrac{1}{2}(1 - \phi)q_4]\theta_{CO}^4 \\ & + [\tfrac{1}{3}(1 - \phi)q_5 + \tfrac{3}{4}(1 - 2\phi)q_4]\theta_{CO}^3 \\ & + [-\tfrac{2}{3}(1 - 2\phi)q_5 - \phi q_6]\theta_{CO}^2 \\ & + [-\tfrac{1}{2}(1 - 2\phi)q_6 - \phi q_5]\theta_{CO} - \phi q_6. \end{aligned} \qquad \text{(B.3a)}$$

$$\begin{aligned} b = {} & [\tfrac{1}{4}\alpha q_4]\theta_{CO}^5 + [\tfrac{1}{2}(1 - \alpha - 2\phi)q_4]\theta_{CO}^4 \\ & + [-\tfrac{1}{2}\alpha q_6 + \tfrac{1}{3}(1 - \alpha - 2\phi q_5) + \tfrac{3}{2}\phi q_4]\theta_{CO}^3 \\ & + [-\tfrac{4}{3}\phi q_5]\theta_{CO}^2 + [\phi q_6]\theta_{CO} \end{aligned} \qquad \text{(B.3b)}$$

$$\begin{aligned} c = {} & [\tfrac{1}{4}\alpha q_4]\theta_{CO}^5 + [\tfrac{1}{2}\phi q_4]\theta_{CO}^4 \\ & + [-\tfrac{1}{2}\alpha q_6 - \tfrac{1}{3}\phi q_5]\theta_{CO}^3 \end{aligned} \qquad \text{(B.3c)}$$

$$q_4 = 4\alpha^2 \quad q_5 = -6\alpha(\alpha + 1) \quad q_6 = 2(\alpha + 1)^2 \qquad \text{(B.3d)}$$

A γ_r versus β_r bifurcation map is constructed (with all other parameters fixed) by varying θ_{CO} as a parameter between 0 and 1, solving for β_r in (B.2) (considering both roots), and then γ_r in (B.1). A y versus β_r map is constructed by solving Eqs. (13) and (B.1) for y and β_r while varying θ_{CO} as a parameter (with all other parameters fixed). IMSL sub routine DNEQNF was used.

b. Isola Variety and Boundary–Isola Transition for Model I

The isola variety is given by the defining conditions in Eq. (17) (with $\lambda \equiv y$). This transition has the defining conditions in Eq. (18). The function F and $\partial F/\partial\theta_{CO}$ are given by Eqs. (13) and (B.1), respectively. The derivative of F with respect to y is given by

$$\begin{aligned} \frac{\partial F}{\partial y} = {} & [\alpha^2\gamma(2E_\alpha + E_\gamma)]\theta_{CO}^4 \\ & + [\alpha\{\beta E_\beta + (\beta + 1)E_\alpha \\ & - 2\gamma[(\alpha + 1)(E_\alpha + E_\gamma) + \alpha E_\alpha]\}]\theta_{CO}^3 \\ & + [\gamma(\alpha + 1)[[(\alpha + 1)E_\gamma + 2\alpha E_\alpha] \\ & + \beta[(\beta + 1 - \alpha)E_\beta + \beta E_\beta - \alpha E_\alpha] \\ & - \phi(\beta + 1)[(\beta + 1)E_\phi + 2\beta E_\beta]]\theta_{CO}^2 \\ & + [-\beta\{E_\beta[\beta - 2\phi(\beta + 1)] \\ & + \beta E_\beta - 2\phi[(\beta + 1)E_\phi + \beta E_\beta]\}]\theta_{CO} \\ & - \phi\beta^2(E_\phi + 2E_\beta) = 0. \end{aligned} \qquad \text{(B.4)}$$

The locus of the BI points in the ϕ_r versus γ_r plane is found as follows. For fixed values of α_r, E_α, E_β, E_γ, and E_ϕ, β is solved for in (B.2) (considering both roots) and γ is calculated using (B.1). These results, denoted by $\beta_\pm$ and $\gamma_\pm$, are substituted into (B.4), giving

$$U[\beta_\pm(\phi_r, \theta_{CO}, \mathbf{p}), \gamma_\pm(\phi_r, \theta_{CO}, \mathbf{p}), \theta_{CO}, \mathbf{p})] = 0, \qquad \text{(B.5)}$$

where $\mathbf{p}$ is a vector of parameters containing α_r, E_α, E_β, E_γ, and E_ϕ. The solution procedure is to vary θ_{CO} as a parameter and solve numerically for ϕ_r in (B.5) for a fixed $\mathbf{p}$ and $y = y_1$.

The isola points are determined by fixing α_r, ϕ_r, E_α, E_γ, and E_ϕ, and then solving (B.5) for y by varying θ_{CO} as a parameter.

c. Hysteresis Variety and Boundary–Hysteresis Transition for Three-Step Model I

The hysteresis variety is solved in the same manner as the isola variety in (b). The only difference is that the following second derivative of the steady-state function (F) with respect to θ_{CO} replaces Eq. (B.4):

$$\begin{aligned} \frac{\partial^2 F}{\partial\theta_{CO}^2} = {} & 12\theta_{CO}^2[\alpha^2\gamma] \\ & + 6\theta_{CO}[\alpha(\beta + 1) - 2\alpha\gamma(\alpha + 1)] \\ & + 2[\gamma(\alpha + 1)^2 + \beta(\beta + 1 - \alpha) \\ & - \phi(\beta + 1)^2] = 0. \end{aligned} \qquad \text{(B.6)}$$

The locus of BH points in the ϕ_r-γ_r plane is calculated as follows. For a fixed $\mathbf{p}$ and $y = y_1$, θ_{CO} is varied as a parameter. Then $\beta_\pm$ and $\gamma_\pm$ are substituted into (B.6). ϕ_r is then solved for each θ_{CO}.

d. Pitchfork Transition for the Three-Step Model I

Equations (13), (B.1), (B.4), and (B.6) describe this transition. These can be reduced to two equations in the following manner. γ is solved for in Eq. (B.1). The resulting expression is substituted into (B.6). ϕ appears linearly in this result, the solution for which gives

$$\phi = \frac{q_7[\theta_{CO}^2 q_1 - 2\theta_{CO}\beta(\beta + 1 - \alpha) + \beta^2] + q_8[6\theta_{CO}\alpha(\beta + 1) + 2\beta(\beta + 1 - \alpha)]}{2(\beta + 1)[(\beta + 1)q_8 - ((\beta + 1)\theta_{CO} - \beta)q_7]} \quad \text{(B.7)}$$

where

$$q_7 = \theta_{CO}^2 q_1 + \theta_{CO} q_2 + \theta_{CO} \quad \text{(B.8a)}$$

$$q_8 = \theta_{CO}[\theta_{CO}^2 q_4 + \theta_{CO} q_5 + \theta_{CO} q_6]. \quad \text{(B.8b)}$$

Substitution of γ and ϕ into Eqs. (13) and (B.4) gives two equations which are solved for β_r and y while varying θ_{CO} as a parameter (with all other parameters fixed).

e. Double–Isola Transition for the Three-Step Model I

This transition is defined by Eqs. (13), (B.1), (B.4) and $\det(d^2F) = 0$, which is defined in Eq. (19). The term $\partial^2 F/\partial\theta_{CO}^2$ is given by Eq. (B.6). $\partial^2 F/\partial y^2$ is determined by differentiating Eq. (B.4) with respect to y, and is provided elsewhere (*51*). $\partial^2 F/\partial y \partial\theta_{CO}$ is determined by differentiating Eq. (B.4) with respect to θ_{CO} (*51*). These four simultaneous equations are solved in a manner similar to the procedure described in (b) and (c). The two possible solutions for β (from (B.2)) and γ (from (B.1)) are substituted into Eqs. (13) and $\det(d^2F) = 0$. θ_{CO} is then varied as a parameter and y and ϕ_r are solved for numerically.

APPENDIX C

Apparent Activation Energy Derivation for the Three-Step Model I

Application of the expression for ε_a (Eq. (29)) to the approximation of three-step model in the CO inhibition regime (Eqs. (26) and (27)) proceeds as follows. Equations (28), (29), and (30) give

$$\varepsilon_a = \varepsilon_3 - \left(\frac{1}{X_\gamma(1 - \theta_{CO})^2}\right) \frac{d}{d\left(\frac{1}{y}\right)}[X_\gamma(1 - \theta_{CO})^2], \quad \text{(C.1)}$$

where $X_\gamma = \exp\{E_\gamma(1 - 1/y)\}$, and $E_\gamma = -\varepsilon_3$. Equation (C.1) then simplifies to Eq. (31). Using Eq. (32) for θ_{CO}, we get Eq. (33), where

$$\frac{d(\Delta(y))}{d\left(\frac{1}{y}\right)} = 2(\beta + 1 - 2\alpha\gamma)[-\beta E_\beta + 2\alpha\gamma(E_\alpha + E_\gamma)] - 4\alpha\gamma[(E_\alpha + E_\gamma)(\alpha\gamma - \beta) + \beta E_\beta - \alpha\gamma(E_\alpha + E_\gamma)]. \quad \text{(C.2)}$$

APPENDIX D

Reduction of Model II to a Single Equation Formulation

The two polynomial functions G_1 and G_2 in Eqs. (46) and (47) are combined following the procedure described by Balakotaiah et al. (*58*). The coefficients of θ_O^2 in each equation, $f_{11}(\theta_{CO})$ (Eq. (49a)) and $f_{21}(\theta_{CO})$ (Eq. (49d)), have common roots $\theta_{CO} = 0$ and $1/2\eta$. These roots can introduce extraneous solutions. To avoid this, θ_O is solved for first by eliminating the quadratic term in each equation. The first way is with the operation $G_1(-f_{21}) + G_2(f_{11})$; this gives

$$\theta_O = \frac{f_{21}f_{13} - f_{11}f_{23}}{f_{11}f_{22} - f_{21}f_{12}}. \quad \text{(D.1)}$$

The second way is with the operation $G_1(-f_{23}) + G_2(f_{13})$; this gives

$$\theta_O = \frac{f_{23}f_{12} - f_{13}f_{22}}{f_{13}f_{21} - f_{23}f_{11}}. \quad \text{(D.2)}$$

Equations (D.1) and (D.2) are equated to give the single function of one intrinsic state variable (θ_{CO}), as provided in Eq. (50). Solutions of Eq. (50) are determined to be identical to solutions of the original set of three equations (37)–(40).

ACKNOWLEDGMENTS

This research was supported by a type G starter grant from ACS-PRF (no. 18322-G5) and a grant from DOE Basic Energy Sciences (no. DE-FGO2-87ER13772).

REFERENCES

1. Harold, M. P., and Garske, M. E., *J. Catal.* **127,** 553 (1990).
2. Kummer, J. T., *J. Phys. Chem.* **90,** 4747 (1986).
3. Engel, T., and Ertl, G., *Adv. Catal.* **28,** 1 (1979); *J. Chem. Phys.* **69,** 1267 (1978).
4. Razon, L. F., and Schmitz, R. A., *Catal. Rev. Sci. Eng.* **28,** 89 (1986).
5. Golchet, A., and White, J. M., *J. Catal.* **53,** 266 (1978).
6. Taylor, J. L., Ibbotson, D. E., and Weinberg, W. H., *J. Catal.* **62,** 1 (1980).
7. Sung, B. P., Sc. dissertation, Massachusetts Institute of Technology (1981).
8. Ertl, G., Norton, P. R., and Rüstig, J., *Phys. Rev. Lett.* **49,** 177 (1982).
9. Cox, M. P., Ertl, G., and Imbihl, R., *Phys. Rev. Lett.* **54,** 1725 (1985).
10. Norton, P. R., Bindner, P. E., Griffiths, K., Jackman, T. E., Davies, J. A., and Rüstig, *J. Chem. Phys.* **80,** 3859 (1984).
11. Imbihl, R., Cox, M. P., Ertl, G., Muller, H., and Brenig, W., *J. Chem. Phys.* **83,** 1578 (1985).
12. Yeates, R. C., Turner, J. E., Gellman, A. J., and Somorjai, G. A., *Surf. Sci.* **149,** 175 (1985).
13. Beusch, P., Fieguth, P., and Wicke, E., *Chem. Ing. Technik* **44,** 445 (1972).
14. Dauchot, J. P., and Van Cakenberghe, J., *Nature (London) Phys. Sci.* **246,** 61 (1973).
15. Plichta, R. T., and Schmitz, R. A., *Chem. Eng. Commun.* **3,** 387 (1979).
16. Turner, J. E., Sales, B. C., and Maple, M. B., *Surf. Sci.* **103,** 54 (1981).
17. Haaland, D. M., and Williams, J. L., *J. Catal.* **76,** 450 (1982).
18. Harold, M. P., and Luss, D., *Chem. Eng. Sci.* **40,** 39 (1985).
19. Lindstrom, T. H., and Tsotsis, T. T., *Surf. Sci.* **171,** 349 (1986).
20. Kaul, D. J., and Wolf, E. E., *J. Catal.* **91,** 216 (1985).
21. Burrows, V. A., Sundaresan, S., Chabal, Y. J., and Christmann, S. B., *Surf. Sci.* **160,** 122 (1985).
22. Möller, P., Wetzl, K., Eiswirth, M., and Ertl, G., *J. Chem. Phys.* **85,** 5328 (1986).
23. Eisworth, M. and Ertl, G., *Surf. Sci.* **177,** 90 (1986).
24. Eisworth, M., Krischer, K., and Ertl, G., *Surf. Sci.* **202,** 565 (1988).
25. Sales, B. C., Turner, J. E., and Maple, M. B., *Surf. Sci.* **114,** 381 (1982).
26. Oh, S. H., Fisher, G. B., Carpenter, J., and Goodman, D. W., *J. Catal.* **100,** 360 (1986).
27. Goodman, D. W., and Peden, C. H. F., *J. Phys. Chem.* **90,** 4839 (1986).
28. Berlowitz, P. J., Peden, C. H. F., and Goodman, D. W., *J. Phys. Chem.* **92,** 5213 (1988).
29. McCarthy, E., Zahradnik, J., Kuczynski, G. C., and Carberry, J. J., *J. Catal.* **39,** 29 (1975).
30. Cant, N. W., Hicks, P. C., and Lennon, B. S., *J. Catal.* **54,** 372 (1978).
31. Garske, M. E., and Harold, M. P., *in* "N. A. Catalysis Soc. Meeting, Dearborn, MI (1989)."
32. Graham, W. R. C., and Lynch, D. T., *AIChE J.* **33,** 792 (1987).
33. Cardosa, M. A. A., and Luss, D., *Chem. Eng. Sci.* **24,** 1699 (1969).
34. Harold, M. P., and Luss, D., *Ind. Eng. Chem. Res.* **26,** 2099 (1987).
35. Lindstrom, T. H., and Tsotsis, T. T., *Surf. Sci.* **146,** L569 (1984).
36. Kaul, D. J., Sant, R., and Wolf, E. E., *Chem. Eng. Sci.* **42,** 1399 (1987).
37. Harold, M. P., Sheintuch, M., and Luss, D., *Ind. Eng. Chem. Res.* **26,** 786 (1987).
38. Eigenberger, G., *Chem. Eng. Sci.* **33,** 1255 (1978).
39. Herz, R. K., and Marin, S. P., *J. Catal.* **65,** 281 (1980).
40. Bykov, V. I., Yablonski, C. G., and Elokhin, V. I., *Surf. Sci.* **107,** L334 (1981).
41. Goodman, M. G., Cutlip, M. B., Kenney, C. N., Morton, W., and Mukesh, D., *Surf. Sci.* **120,** L453 (1982).
42. Harold, M. P., Sheintuch, M., and Luss, D., *Ind. Eng. Chem. Res.* **26,** 794 (1987).
43. Voltz, S. E., Morgan, C. R., Liederman, D. M., and Jacob, S. M., *Ind. Eng. Chem. Prod. Res. Dev.* **12,** 294 (1973).
44. Shishu, R. C., and Kowalczyk, L. S., *Plat. Met. Rev.* **18,** 8 (1974).
45. Nicholas, D. M., and Shah, Y. T., *Ind. Eng. Prod. Res. Dev.* **15,** 35 (1976).
46. Hori, G. K., and Schmidt, L. D., *J. Catal.* **38,** 335 (1975).
47. Hegedus, L. L., Oh, S. H., and Baron, K., *AIChE J.*, **32,** 632 (1977).
48. Balakotaiah, V., and Luss, D., *Chem. Eng. Sci.* **37,** 1611 (1982).
49. Balakotaiah, V., and Luss, D., *Chem. Eng. Sci.*, **38,** 1709 (1983).
50. Golubitsky, M., and Schaeffer, D. G., "Singularities and Groups in Bifurcation Theory," Vol. 1. Springer-Verlag, New York (1985).
51. Garske, M. E., Ph.D. dissertation, University of Massachusetts (1990).
52. Heyne, H., and Tompkins, F. C., *Proc. R. Soc. London Ser. A* **292,** 460 (1966).
53. Monroe, D. R., and Merrill, R. P., *J. Catal.* **65,** 461 (1980).
54. Langmuir, I., *Trans. Faraday Soc.* **17,** 621 (1921/1922).
55. White, J. M., and Golchet, A. J., *J. Chem. Phys.* **61,** 5744 (1977).
56. Matsushima, T., Almy, D. B., and White, J. R., *Surf. Sci.* **67,** 89 (1977).
57. Dwyer, S. M., and Bennett, C. O., *J. Catal.* **75,** 275 (1982).

58. Balakotaiah, V., Luss, D., and Keyfitz, B. L., *Chem. Eng. Commun.* **36,** 121 (1985).
59. McCabe, R. W., and McCready, D. F., *J. Phys. Chem.* **90,** 1428 (1986).
60. Bonzel, H. P., and Ku, R., *J. Vacuum Sci. Tech.* **9,** 663 (1972).
61. Conrad, H., Ertl, G., and Kuppers, J., *Surf. Sci.* **76,** 323 (1978).
62. McCabe, R. W., and Schmidt, L. D., *Surf. Sci.* **66,** 101 (1977).
63. Gorte, R., and Schmidt, L. D., *Surf. Sci.* **76,** 559 (1978).
64. Dorling, T. A., and Moss, R. L., *J. Catal.* **7,** 378 (1967).
65. Yao, H. C., Sieg, M., and Plummer, H. K., Jr., *J. Catal.* **59,** 365 (1979).
66. Lennard-Jones, J. E., *Trans. Faraday Soc.* **28,** 333 (1932).
67. Ceyer, S., *Science,* 133 July, (1990).